

This is a postprint version of the following published document:

Zapardiel, Diego; García-Salaberri, Pablo A. (2022). Modeling the interplay between water capillary transport and species diffusion in gas diffusion layers of proton exchange fuel cells using a hybrid computational fluid dynamics formulation, *Journal of Power Sources*, v. 520, 230735.


DOI: <https://doi.org/10.1016/j.jpowsour.2021.230735>

© 2021 Elsevier Ltd. All rights reserved.



This work is licensed under a [Creative Commons AttributionNonCommercialNoDerivatives 4.0 International License](https://creativecommons.org/licenses/by-nc-nd/4.0/)

# Modeling the interplay between water capillary transport and species diffusion in gas diffusion layers of proton exchange fuel cells using a hybrid computational fluid dynamics formulation

Diego Zapardiel and Pablo A. García-Salaberri\* 

Department of Thermal and Fluids Engineering, Universidad Carlos III de Madrid, 28911 Leganés, Spain

\* Correspondence: pagsalab@ing.uc3m.es; Tel.: +34-916249407

**Abstract:** Improved modeling of the membrane electrode assembly (MEA) and operation is essential to optimize proton exchange fuel cells (PEFCs). In this work, a hybrid model, which includes a pore network formulation to describe water capillary transport and a continuum formulation to describe gas diffusion, is presented. The model is validated with previous data of carbon-paper gas diffusion layers (GDL), including capillary pressure curve, relative effective diffusivity,  $g(s)$ , and saturation profile. The model adequately captures the increase of capillary pressure with compression, the nearly cubic dependency of  $g(s)$  on average saturation,  $s^{\text{avg}}$ , and the shape of the saturation profile in conditions dominated by capillary fingering (e.g., running PEFC at low temperature). Subsequently, an analysis is presented in terms of the area fraction of water at the inlet and the outlet of the GDL,  $A_w^{\text{in}}$  and  $A_w^{\text{out}}$ , respectively. The results show that gas diffusion is severely hindered when  $A_w^{\text{in}}$  is exceedingly high (>80%), a situation that can arise due to the bottleneck created by flooded interfacial gaps. Furthermore, it is found that  $s^{\text{avg}}$  increases with  $A_w^{\text{out}}$ , reducing the GDL effective diffusivity. Overall, the work shows the importance of an appropriate design of MEA porous media and interfaces in PEFCs.

**Keywords:** capillary transport; diffusive transport; gas diffusion layer; hybrid modeling; polymer electrolyte fuel cell

---

## 1. Introduction

Proton exchange fuel cell (PEFC) technology has experienced an increasing deployment in both mobile and stationary power-source applications in the last decade, as an eco-friendly alternative to fossil fuel devices [1,2]. However, in the current energy transition period, it is still necessary to minimize the costs and increase the durability and efficiency of PEFCs for its widespread introduction into the

market [3–5]. This task requires a combined work on components design, production, assembly and operation to achieve the stringent performance and durability targets set for PEFCs in the upcoming decades [6,7]. As a result, a large research activity has been devoted to the improvement of the components of the membrane electrode assembly (MEA), namely the gas diffusion layer (GDL), the micro-porous layer (MPL), the catalyst layer (CL) and the polymer membrane (PEM) [8–11].

Adequate management of multiphase transport of water (i.e., water vapor, liquid water and water dissolved in ionomer) is a transversal aspect to all the porous layers of the MEA in order to achieve good PEM hydration and reduced mass-transport losses [12]. In this regard, four lines of innovation with high interest in the literature can be distinguish: (i) ordered 3D GDLs, (ii) graded design of GDLs and MPLs, (iii) nano-structured and ionomer-free CLs, and (iv) highly conductive PEMs at low humification [13]. Recent works presented in the literature are reviewed below. Niblett et al. [14,15] (2019,2020) presented 3D printed micro-structures as optimized and cost-saving thin porous media to be used as GDLs, leading to improved effective electrical conductivity and two-phase properties, higher uniformity of reactant distribution and reduced contact resistances. Shrestha et al. [16] (2019) developed a novel MPL with spatially-graded PTFE content, which reduced water flooding in the cathode GDL, thereby increasing performance at high current densities ( $I \geq 1 \text{ A cm}^{-2}$ ). Qi et al. [17] (2021) produced free-standing and ionomer-free nanothrough-like cathode CLs with low Pt loading ( $42 \mu\text{g cm}^{-2}$ ), which showed a peak power density of  $0.936 \text{ W cm}^{-2}$  at  $80 \text{ }^\circ\text{C}$  and extremely low degradation after 5000 cycles. The enhanced performance was explained by reduced mass-transport losses due to the absence of ionomer, the porous structure of the thin CLs, and the facilitated water management due to the super-hydrophobic character of the generated biomimetic architecture. Kusoglu et al. [18] (2019) presented a perfluorinated PEM with multiacid side chains as an alternative to common perfluorosulfonic acid PEMs, which significantly increased proton conductivity at low-to-medium relative humidities ( $\text{RH} = 20 - 70\%$ ).

In this context, a better understanding of the interplay between gas diffusion and liquid water transport in the MEA is still necessary. This is especially relevant at the cathode because of water generation in this compartment, the lower mass diffusivity of oxygen and the sluggish kinetics of the oxygen reduction reaction (ORR) (see,e.g.,[8,19,20]). Most experimental and numerical works have focused on transport in the GDL and the MPL, with an increasing attention to the interfaces of MEA components and the CL in the last years [21,22]. Zenyuk et al. [23] (2015) investigated ex-situ the effect of the rib/channel geometry on liquid water distribution in GDLs under different compression ratios (CR) using X-ray computed tomography (X-CT). They observed that liquid water was uniformly distributed under the rib and the channel areas at low CRs. However, water invasion was predominantly concentrated under the channel area at high CRs due to the larger pore size

(lower capillary resistance) prevailing in this region. García-Salaberri et al. [24] (2015) used the lattice Boltzmann method (LBM) to examine the effect of water distribution on effective diffusivity in X-CT images of carbon-paper GDLs. They concluded that the resistance of water to gas transport in thin GDLs is largely influenced by the peak water saturation and not only the average water saturation. In a subsequent work, García-Salaberri et al. [25] (2015) examined the difference between local and global effective transport properties in carbon-paper GDLs. They found that the relative effective diffusivity depends on water saturation through a power-law of the form  $(1 - s)^n$ , being the local saturation exponent,  $n_l \approx 2$ , lower than the global saturation exponent (i.e., of the full layer),  $n_g \approx 3 - 4.5$ . This fact was explained by the effect of the blockage of non-uniform saturation distribution across the material [24]. More recently, Carrere & Prat [26] (2019) presented a comprehensive pore-network model (PNM) to simulate liquid water transport in the cathode GDL. Their study identified four regimes of water transport: (i) dry regime, (ii) condensation-dominated regime, (iii) liquid injection-dominated regime, and (iv) mixed regime where both capillary transport and condensation are important. Xu et al. [27] examined in-situ water transport in the GDL/MPL at 40 °C and 80 °C using subsecond and submicron X-CT. They found that water transport is dominated by capillary fingering and phase-change-induced flow at 40 °C and 80 °C, respectively. Chen et al. [28] (2021) developed a LBM model to simulate coupled processes in the cathode CL, including oxygen diffusion, electrochemical reaction and two-phase flow. They observed that liquid water first fills small pores surrounding large pores, and then is transported into large pores. At this stage, liquid water forms continuous flow paths, following a capillary fingering mechanism, as in the GDL and the MPL. They concluded that increasing the hydrophobicity of the cathode CL can alleviate water flooding and promote water evaporation, thus facilitating oxygen transport toward active catalytic sites.

The works referenced above reflect the importance of optimizing water management and improving oxygen diffusion in PEMFCs, a task which is inherently coupled with MEA design and operation. In this regard, numerical modeling plays a key role to examine transport in the small scales of the MEA and provide insight for better designs. With this aim, a hybrid model, which combines a discrete formulation to model capillary transport and a continuum formulation to model gas diffusion in GDLs, is presented, validated and analyzed. The formulation is built upon the composite model recently presented by Garcia-Salaberri [29] to model diffusion and convection in thin porous transport layers by combining a microscopic PN model and a macroscopic control volume (CV) mesh. The organization of the paper is as follows. In Section 2, the numerical model is presented, including a description of coupled capillary transport and gas diffusion, as well as the output parameters. In Section 3, the results are discussed, including a model validation with previous experimental data and

a parametric analysis of the effect of water invasion on gas diffusion in GDLs. Finally, the conclusions and future work are presented in Section 4.

## 2. Model formulation

The present GDL model is based on the CV mesh representation previously presented by Garcia-Salaberri et al. [29], but removing connectors to simplify the formulation and reduce computational cost. CVs are used to determine local effective transport properties and model discrete capillary transport of water. This approach overcomes the lack of separation between pore and layer scales, which prevents the definition of an REV across the thickness (barely spanning around ten pore sizes) [30,31]. Hence, the formulation is divided into two sub-models: (i) a microscopic model, which describes transport and geometry within each CV, and (ii) a macroscopic model, which describes transport throughout the CV mesh. Specifically, the microscopic model makes use of a structured PN to determine structural and transport properties at the pore/throat scale in each CV, namely the local characteristic pore radius,  $r_{c,l}$ , the local porosity,  $\varepsilon_l$ , and the local effective diffusivity tensor,  $\overline{\overline{D}}_l^{\text{eff}}$  (see [29] for further details). The macroscopic model embeds the information of the microscopic model to determine global structural properties, including the average porosity,  $\varepsilon^{\text{avg}}$ , and the volume-average characteristic pore radius,  $r_c^{\text{avg}}$ , and to solve for water capillary transport and gas diffusion at the layer or material scale, among other possible transport processes.

Two GDLs, uncompressed and compressed (compression ratio, CR = 30%) Toray TGP-H-120 with 10% PTFE by weight were examined in this work. Examples of the PN and CV mesh of both GDLs are shown in Figure 1, together with their experimental pore size distributions (PSD). Relevant characteristics of both GDLs are listed in Table 1. The PSDs (i.e., the volume fraction of pores that have radius  $r$ ), used as input parameter to the microscopic model, were extracted from those reported by Zenyuk et al. [32] using log-normal bimodal distributions of the form

$$\text{PSD}(r) = \sum_{k=1,2} f_{r,k} \left\{ \frac{1}{r\sigma_k\sqrt{2\pi}} \exp \left[ -\frac{(\ln r - \ln r_{0,k})^2}{2\sigma_k^2} \right] \right\} \quad (1)$$

where  $f_{r,k}$  is the fraction of pores that compose the distribution  $k$ , and  $r_{0,k}$  and  $\sigma_k$  are the characteristic radius and standard deviation of the distribution  $k$ , respectively.

To capture the effect of heterogeneities in the continuum formulation,  $\beta = 27$  computational cells, three in each spatial direction, were included in every CV (see mesh resolution study in Supplementary Material). This level of resolution showed negligible variations in diffusion simulations under two-phase conditions compared to denser meshes with  $\beta = 64$  cells. In fact, the absolute difference between using  $\beta = 8 - 27$  cells per CV was not very significant. In both cases, the variation of the relative blockage of water in the through-plane (TP) direction is well correlated by a power law of the

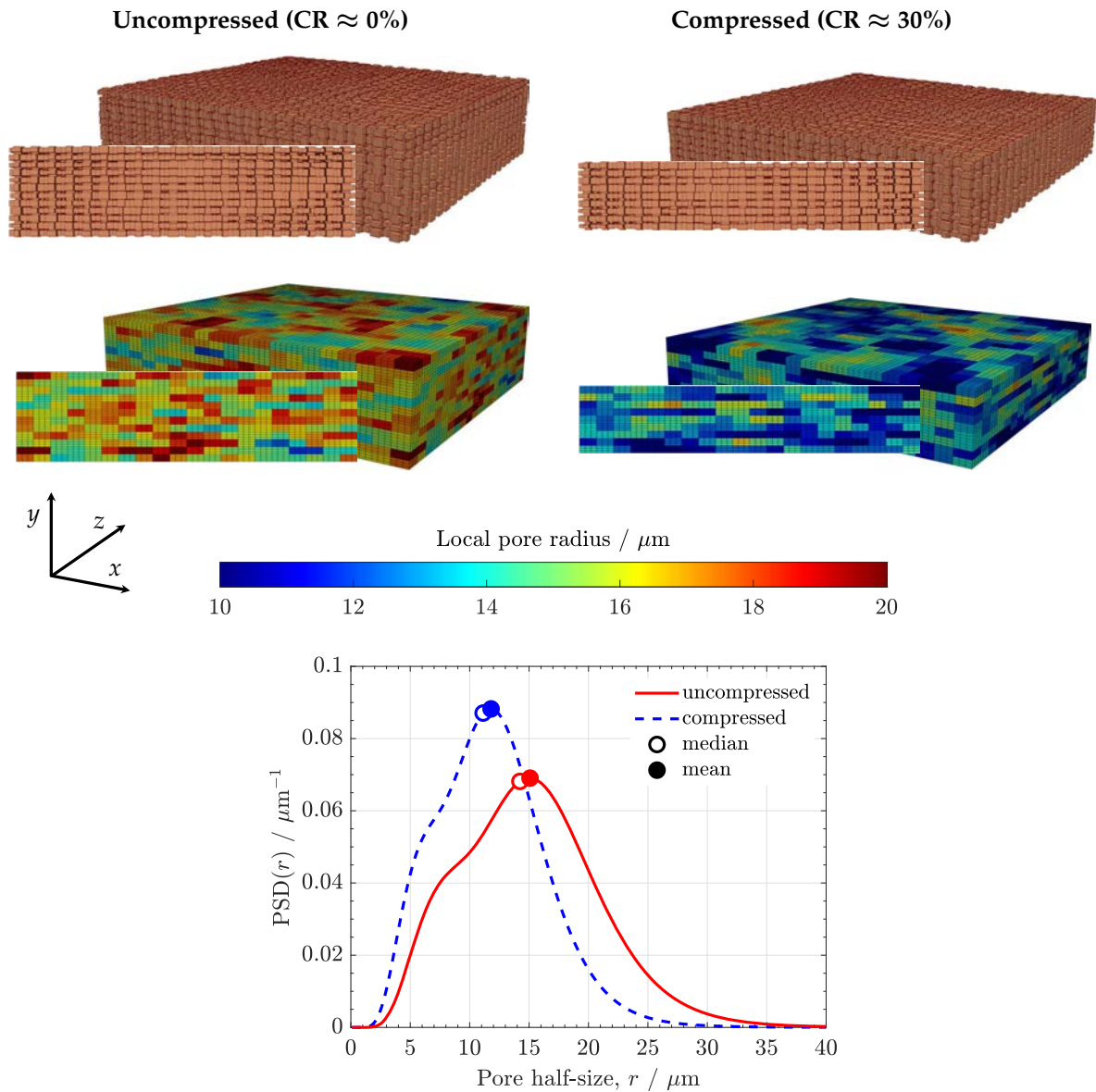


**Figure 1.** (up) Structured PN and CV mesh of the uncompressed and 30% compressed Toray TGP-H-120 GDLs, showing the coordinate system. The CVs are colored according to the local characteristic pore radius,  $r_{c,l}(x, y, z)$ . The average pore radius of the uncompressed and compressed samples are  $r_c^{\text{avg}} \approx 15 \mu\text{m}$  and  $11.7 \mu\text{m}$ , respectively, and the selected mesh density per CV is  $\beta = 27$ . (down) Pore size distributions of the GDLs,  $\text{PSD}(r)$ , indicating the mean and the median.

form  $g_{TP} = (1 - s^{avg})^{n_g}$ , with  $n_g \approx 3 - 4$ . A denser mesh is needed to accurately capture the drop of GDL effective diffusivity when water blockage is controlled by thin highly saturated regions, spanning only 1-2 CVs in thickness. The mesh densities achieved with the hybrid model are around one order of magnitude larger than 3D macro-homogeneous models, typically including 10-20 computational cells across the thickness and below channels and ribs [33]. The number of cells could be reduced by including more than one pore in each CV in the  $x - z$  plane, while preserving the number of CVs (i.e., computational cells) in the thickness direction to capture finite-size effects [30,31]. Furthermore, the hybrid model offers a rather easy implementation of microstructural heterogeneities in CFD codes used in engineering applications, as well as a fast computation of continuum-based equations with state-of-the-art solvers. Here, the model was implemented in the commercial code ANSYS FLUENT 2020. User defined functions (UDFs) were used to customize different aspects of the numerical model (spatially-varying effective properties, boundary conditions, etc.) and to implement the capillary invasion algorithm in parallel. Simulations were run with four processors on a workstation equipped with 40 cores Intel Xeon 6230 at 2.1 Ghz and 256 GB RAM.



**Table 1.** Parameters used in the hybrid model of the uncompressed/compressed TGP-H-120 GDLs. The conditions corresponding to the baseline case are underlined.

Parameter	Symbol	Value	Reference
Temperature, gas-phase pressure, RH <sup>1</sup>	$T, p_{\text{gas}}, \text{RH}$	70 °C, 1 bar, 1	[33,34]
Inlet capillary pressure	$p_c^{\text{in}}$	0 – 15 kPa	–
PSD fraction	$f_{r,1}, f_{r,2}$	0.461, 0.539	[32]
PSD characteristic radius	$r_{0,1}, r_{0,2}$	10.3, 16.6 $\mu\text{m}$ /8.1, 13 $\mu\text{m}$	[32]
PSD standard deviation	$\sigma_1, \sigma_2$	0.457, 0.255	[32]
Throat, pore size scaling parameter	$\Gamma_t, \Gamma_p$	1.05, 1.02	Assumed
CV characteristic size	$L_{CV,x} \times L_{CV,z} \times L_{CV,y}$	62 $\times$ 62 $\times$ 27 $\mu\text{m}^3$	–
Computational cells per CV	$\beta$	27	–
GDL thickness (number of CVs)	$\delta_{\text{gdl}}(N_{CV,y})$	324(12)/243(9) $\mu\text{m}$	[32,35,36]
MPL thickness <sup>1</sup>	$\delta_{\text{mpl}}$	50 $\mu\text{m}$	[37–40]
Representative domain size	$L_x \times L_z$	<u>1.24 <math>\times</math> 1.24 <math>\text{mm}^2</math></u> 1.24 $\times$ 0.62 $\text{mm}^2$ 1.24 $\times$ 2.48 $\text{mm}^2$	–
Inlet reservoir thickness	$\delta_{\text{res}}^{\text{in}}$	50 $\mu\text{m}$	–
Characteristic fiber diameter	$d_f$	10 $\mu\text{m}$	[41,42]
Average porosity	$\varepsilon^{\text{avg}}$	$\approx$ 0.75/0.57	[30,32,43]
Average characteristic pore radius	$r_c^{\text{avg}}$	$\approx$ 15/11.7 $\mu\text{m}$	[30,32]
Dry norm. effective diffusivity	$D_{\text{TP}}^{\text{eff,dry}}$	$\approx$ 0.24/0.12	–
MPL effective diffusivity <sup>1</sup>	$D_{\text{TP,mpl}}^{\text{eff,wet}}$	0.1 $D_{\text{O}_2,\text{air}}$	[37–40]
Bulk diffusivity	$D$	1 $\text{m}^2 \text{s}^{-1}$	–
Local saturation exponent	$n_l$	1.5, <u>2</u> , 2.5	–
Surface tension	$\sigma$	0.072 $\text{N m}^{-1}$	[33,44]
Contact angle	$\theta$	105 °	[44]
Local residual gas-phase saturation	$s_{l,\text{gas}}^r$	0.2/0.85	Assumed
Local $p_c - s$ invasion parameter	$\eta$	2.5/5.75	Assumed
Inlet concentration	$C^{\text{in}}$	1 $\text{mol m}^{-3}$	–
Outlet concentration	$C^{\text{out}}$	0 $\text{mol m}^{-3}$	–

<sup>1</sup> Parameters used to determine the oxygen diffusion resistance,  $R_{\text{O}_2}^{\text{chcl}}$ , and limiting current density,  $I_{\text{lim}}$  (see Section 2.3).

### 2.1. Capillary transport

Capillary forces dominate quasi-steady-state transport of water in the porous layers of the MEA (GDL/MPL and CL), characterized by small capillary numbers,  $Ca \sim 10^{-8}$ , and a high viscosity ratio,  $M \sim 10$ , thus falling in the capillary-fingering regime [45,46] (see Supplementary Material). As shown in Figure 2, water capillary transport in the GDL is modeled using a discrete PN algorithm incorporated into the CV mesh. Throats act as active elements, controlling the invasion process into the CVs, while pore bodies act as passive elements, filled gradually by water (the non-wetting phase,  $p_c = p_l - p_g > 0$ ). Thus, each CV face is characterized by an entry capillary pressure according to the size of the throat that crosses the corresponding face,  $r_{c,t}$ , namely  $p_{c,CV}^{e,\text{up}}, p_{c,CV}^{e,\text{down}}, p_{c,CV}^{e,\text{left}}, p_{c,CV}^{e,\text{right}}, p_{c,CV}^{e,\text{front}}$  and  $p_{c,CV}^{e,\text{back}}$  in 3D. Similarly, the characteristic capillary pressure of a pore body,  $p_{c,CV}$ , is determined



based on its characteristic pore radius,  $r_{c,p}$ . Two different expressions are used to determine  $p_{c,CV}^{e,i}$  and  $p_{c,CV}$ : (i) the classical Washburn equation for straight, cylindrical capillary tubes, and (ii) the Purcell toroid model (modified Washburn equation) [47], previously used by Gostick [44] to provide a better representation of the converging-diverging nature of the fibrous pore space

$$\text{Washburn: } p_{c,CV} = -\frac{2\sigma}{r_c} \quad (2a)$$

$$\text{Purcell: } p_{c,CV} = -\frac{2\sigma}{r_c} \frac{\cos(\theta - \alpha)}{1 + d_f/(2r_c)(1 - \cos \alpha)} \quad (2b)$$

where  $\theta$  is the (volume-average) water-air contact angle of the fibrous microstructure,  $r_c$  is the characteristic pore radius of the throat or pore body (i.e., half-spacing between fibers),  $d_f \approx 10 \mu\text{m}$  is the fiber diameter, and  $\alpha$  is the angle beyond the apex of the curved throat where the maximum meniscus curvature occurs, that is,

$$\alpha = \theta - \pi + \arcsin\left(\frac{\sin \theta}{1 + 2r_c/d_f}\right) \quad (3)$$

The characteristic radii of pores and throats,  $r_c$ , are determined as

$$r_{c,t} = \Gamma_t \frac{H_t + W_t}{2} \quad (4a)$$

$$r_{c,p} = \Gamma_p \frac{r_{p,x} + r_{p,y} + r_{p,z}}{3} \quad (4b)$$

where  $\Gamma_t$  and  $\Gamma_p$  are dimensionless parameters (of order unity), which accounts for the irregular shape of real throats and pores,  $H_t$  and  $W_t$  are the half-height and half-width of throat  $t$ , and  $r_{p,i}$  is the pore radius in  $i$ -direction of pore  $p$  determined from Eq. (1) (see [29] for further details).

Two different scenarios for injecting water into the GDL are examined: (i) capillary pressure-saturation curve,  $p_c - s$ , and (ii) invasion percolation, IP. For  $p_c - s$ , a capillary pressure is imposed at the inlet reservoir,  $p_c = p_c^{in}$ , and invasion evolves until the water front cannot penetrate further into the GDL because the inlet capillary pressure is lower than the entry capillary pressure of the neighboring CVs (i.e.,  $p_c^{in} < p_{c,CV}^e$ ). For IP,  $p_c = p_c^{in}$  is also imposed at the inlet reservoir to vary the interfacial area fraction of invaded CVs at the inlet,  $A_w^{in} = A_w^{in}/A_{gdl}$ , where  $A_{gdl}$  is the platform area of the GDL. Water gradually invades the GDL following the path of lowest capillary resistance until the opposite face is reached (i.e., one CV touching the outlet is invaded). After the breakthrough event, water transport takes place through the same path [44,48,49]. This situation mimic water capillary transport during PEFC operation from the CL to the channel, even though phase change and interactions with the flow in the channel were not considered here [26].

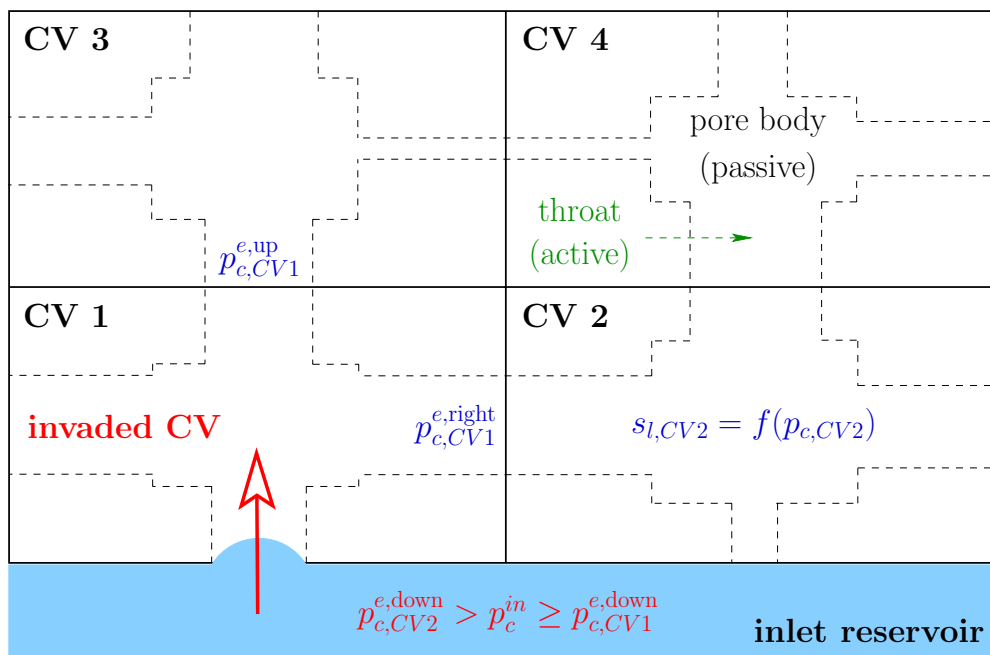


**Figure 2.** Schematic of the CV mesh and the PN geometry within each CV of the GDL, showing the conditions used to model water transport in  $p_c$ -s simulation and initialize IP simulations. The capillary pressure at the inlet reservoir,  $p_c = p_c^{in}$ , and the entry capillary pressures of the throats/faces,  $p_{c,CV}^e$ , are indicated. A CV is invaded of liquid water when  $p_c \geq p_{c,CV}^e$ , being the local saturation in each CV a function of the characteristic capillary pressure of the pore body,  $s_l = f(p_{c,CV})$ .

The numerical algorithm is initialized by labeling all the computational cells that belong to a CV using an identifier, CV's ID, which starts from 1 (0 is reserved for the possible existence of regions that cannot be accessed by liquid water, e.g., a BPP rib). In addition, the six entry capillary pressures (associated with the six throats),  $p_{c,CV}^e$ , and the characteristic capillary pressure (associated with the pore body),  $p_{c,CV}$ , of a certain CV are stored for all the cells that belong to that CV. Hence, all the computational cells in each CV feature the same two-phase properties ( $p_{c,CV}^e$  and  $p_{c,CV}$ ) and behave in a similar way during the iterative process. In each iteration, the following steps are performed to simulate both  $p_c$ -s and IP:

- Step1 A loop is performed over all the computational cells that have been already invaded (including the inlet reservoir and the GDL) to identify the dry cells connected to the invasion front. The entry capillary pressures,  $p_{c,CV}^e$ , of the wet-dry connecting faces (i.e, throats) are evaluated according to the relative position between the wet and the dry cells (up, down, left, right, front or back throats/faces).
- Step 2 For  $p_c - s$  simulations, all the cells marked in Step 1 that have an entry capillary pressure lower than or equal to the actual inlet capillary pressure are determined ( $p_c^e \leq p_c^{in}$ ). Whereas for IP simulations, the cell with the minimum entry capillary pressure,  $p_{c,min}^e$ , is determined. The CV's IDs of the selected cells are stored.

Step 3 The computational cells that have the CV's IDs determined in Step 2 are invaded. That is,  $p_c = p_c^{in}$  is set in all the cells that belong to the CVs identified in Step 3 (possibly more than one CV or none in  $p_c$ -s simulations and only one CV in IP simulations).

Step 4 A pore-filling law is used to account for sub pore-scale phenomena that are not resolved in the method. Based on the work of Gostick et al. [44], the following expression is used to determine the local saturation in each invaded CV (i.e., computational cells inside a CV):

$$s_l = 1 - s_{l,\text{gas}} \left( \frac{p_{c,CV}}{p_c} \right)^\eta \quad (5)$$

where  $s_{l,\text{gas}}$  is the local residual saturation of air (the wetting phase) at the invasion event (i.e.,  $p_c = p_{c,CV}^e$ ), and the parameter  $\eta \in (0, \infty)$  controls the gradual invasion of water with increasing capillary pressure. A larger value of  $\eta$  leads to a sudden invasion of water with capillary pressure ( $s_l \rightarrow 1$  when  $\eta \rightarrow \infty$  since  $p_{c,CV}^e / p_c \leq 1$ ). The minimum physically-sound value is  $\eta \rightarrow 0$ , which leads to an infinitely slow invasion of water with capillary pressure (i.e.,  $s_l \rightarrow 1 - s_{l,\text{gas}}$  when  $\eta \rightarrow 0$ ).

The numerical algorithm is stopped when no more CVs are invaded, i.e., the saturation level in the GDL does not change anymore.

## 2.2. Gas diffusion

Unlike water transport, gas diffusion in the GDL is modeled using a continuum formulation. According to Fick's law, the mass conservation equation of gas species (say oxygen,  $O_2$ ) is given by

$$-\nabla \cdot \left( \overline{\overline{D}}_l^{\text{eff,wet}} \nabla C \right) = 0 \quad (6)$$

where  $C$  is the molar concentration, and  $\overline{\overline{D}}_l^{\text{eff,wet}}$  is the local effective diffusivity tensor under wet (two-phase) conditions.

The microscopic model presented by Garcia-Salaberri [29] is used to determine  $\overline{\overline{D}}_l^{\text{eff,wet}}$ , as given by the following expression

$$\overline{\overline{D}}_l^{\text{eff,wet}} = D \begin{pmatrix} f_{l,x} g_{l,x} & 0 & 0 \\ 0 & f_{l,y} g_{l,y} & 0 \\ 0 & 0 & f_{l,z} g_{l,z} \end{pmatrix} \quad (7)$$

where  $D$  is the bulk mass diffusivity,  $f_{l,i}$  is the local normalized effective diffusivity in  $i$ -direction under dry conditions ( $f_{l,i} = D_{l,i}^{\text{eff,dry}} / D$ ) [29], and  $g_{l,i}$  is the local relative effective diffusivity ( $g_{l,i} =$

$D_{l,i}^{\text{eff,wet}}/D_{l,i}^{\text{eff,dry}}$ ). A power-law relationship was considered in all the space directions,  $g_l = g_{l,i}$ , based on the work of Garcia-Salaberri et al. [25]

$$g_l = (1 - s_l)^{n_l} \quad (8)$$

where  $n_l$  is the local saturation exponent, assumed constant throughout the GDL (see Table 1). The bulk mass diffusivity at the inlet reservoir was set equal to  $D = 1 \text{ m}^2 \text{ s}^{-1}$  (low diffusive resistance,  $D \gg D_l^{\text{eff,wet}}$ ) in order to do not alter the flux distribution in the GDL.

Dirichlet boundary condition are imposed on Eq. (6) at the inlet surface of the reservoir and the outlet surface of the GDL

$$\text{Inlet: } C = C^{\text{in}} \quad (9a)$$

$$\text{Outlet: } C = C^{\text{out}} \quad (9b)$$

where  $C^{\text{in}} = 1 \text{ mol m}^{-3}$  and  $C^{\text{out}} = 0 \text{ mol m}^{-3}$  are the inlet and outlet species concentrations, respectively. Note that the global parameters extracted from the model are independent of the values selected for  $C^{\text{in}}$  and  $C^{\text{out}}$ , as explained in the next section.

### 2.3. Global output parameters

Five volume-average output parameters are analyzed with the numerical model: (i) the average water saturation,  $s^{\text{avg}}$ , (ii) the global effective diffusivity,  $D_{\text{TP}}^{\text{eff,wet}}$ , (iii) the global relative effective diffusivity,  $g_{\text{TP}}$  (and the corresponding saturation exponent,  $n_g$ ), (iv) the global oxygen diffusion resistance,  $R_{\text{O}_2}^{\text{chcl}}$ , and (v) the limiting current density,  $I_{\text{lim}}$ . The expressions used for the calculation of other structural properties, such as the average porosity,  $\varepsilon^{\text{avg}}$ , can be found elsewhere [29].

The average saturation is calculated using the local saturation computed in each CV,  $s_{l,i}$ , according to the following expression

$$s^{\text{avg}} = \frac{\sum_{i=1}^N s_{l,i} V_{l,p,i}}{N V_{\text{CV}}} \quad (10)$$

where  $N$  is the number of CVs in the GDL, and  $V_{l,p}$  and  $V_{\text{CV}}$  are the local pore and total volume of each CV.

The global effective diffusivity in the through-plane direction ( $y$ -direction),  $D_{\text{TP}}^{\text{eff,wet}}$ , is determined using the mean diffusive flux in  $y$ -direction,  $j_y^{\text{avg}}$ , computed in the simulations. Approximating integrals with the trapezoidal rule,  $D_{\text{TP}}^{\text{eff,wet}}$  is given by

$$\frac{D_{\text{TP}}^{\text{eff,wet}}}{D} = \frac{\delta_{\text{gdl}}}{V_{\text{gdl}}} \int_{V_{\text{gdl}}} j_y \text{ d}V = \delta_{\text{gdl}} j_y^{\text{avg}} \approx \frac{\delta_{\text{gdl}}}{N} \sum_{i=1}^{\beta N} -D_{l,y}^{\text{eff,wet}} \left. \frac{\partial C}{\partial y} \right|_i \quad (11)$$

where  $\delta_{\text{gdl}}$  and  $V_{\text{gdl}}$  are the thickness and total volume of the GDL, and  $\beta$  is the number of computational cells per CV.

The value of  $D_{\text{TP}}^{\text{eff,wet}}$  is used to calculate the global relative effective diffusivity,  $g_{\text{TP}}$ , as the ratio between the effective diffusivity under wet ( $s^{\text{avg}} > 0$ ) and dry ( $s^{\text{avg}} = 0$ ) conditions

$$g_{\text{TP}} = \frac{D_{\text{TP}}^{\text{eff,wet}}}{D_{\text{TP}}^{\text{eff,dry}}}, \quad (12)$$

so that the global saturation exponent corresponding to a power law,  $g_{\text{TP}} = (1 - s^{\text{avg}})^{n_g}$ , is equal to

$$n_g = \frac{\log(g_{\text{TP}})}{\log(1 - s^{\text{avg}})} \quad (13)$$

where  $s^{\text{avg}}$  is given by Eq. (10).

The overall oxygen diffusion resistance from the channel to the CL,  $R_{\text{O}_2}^{\text{chl}}$ , is equal to

$$R_{\text{O}_2}^{\text{chl}} = R_{\text{O}_2,\text{gdl}} + R_{\text{O}_2,\text{mpl}} \quad (14)$$

where  $R_{\text{O}_2,\text{gdl}}$  and  $R_{\text{O}_2,\text{mpl}}$  are the diffusion resistances across the GDL and the MPL, respectively. Both resistances are given by the following expressions

$$R_{\text{O}_2,\text{gdl}} = \frac{\delta_{\text{gdl}}}{D_{\text{TP}}^{\text{eff,wet}}}; \quad R_{\text{O}_2,\text{mpl}} = \frac{\delta_{\text{mpl}}}{D_{\text{mpl}}^{\text{eff,wet}}} \quad (15)$$

Here,  $D_{\text{TP}}^{\text{eff,wet}} = (D_{\text{TP}}^{\text{eff,wet}}/D)D_{\text{O}_2,\text{air}}$  and  $D_{\text{mpl}}^{\text{eff,wet}}$  are the effective diffusivities of oxygen through the GDL and the MPL, respectively, and  $\delta_{\text{mpl}}$  is the MPL thickness. According to previous works [37–40], it was considered  $\delta_{\text{mpl}} \approx 50 \mu\text{m}$  and  $D_{\text{mpl}}^{\text{eff,wet}} \approx 0.1D_{\text{O}_2,\text{air}}$ , as representative values. The molecular diffusivity of oxygen in air,  $D_{\text{O}_2,\text{air}}$ , depends on temperature,  $T$ , and gas-phase pressure,  $p_{\text{gas}}$ , as follows [50]

$$D_{\text{O}_2,\text{air}} = 2.65 \times 10^{-5} \left( \frac{T}{333} \right)^{1.5} \left( \frac{10^5}{p_{\text{gas}}} \right) \quad [\text{m}^2 \text{s}^{-1}] \quad (16)$$

A typical PEFC operating temperature and pressure of  $T = 70 \text{ }^\circ\text{C}$  and  $p_{\text{gas}} = 1 \text{ bar}$ , respectively, were considered in this work [33,34] (see Table 1).

The limiting current density,  $I_{\text{lim}}$ , corresponds to conditions of oxygen starvation in the cathode CL,  $C_{\text{O}_2,\text{cl}} = 0$  [51]. According to Faraday's law,  $I_{\text{lim}}$  is given in terms of  $R_{\text{O}_2}^{\text{chl}}$  as

$$I_{\text{lim}} = 4Fj_{\text{O}_2,y}^{\text{avg}} = 4F \frac{C_{\text{O}_2,\text{ch}}}{R_{\text{O}_2}^{\text{chl}}} \quad (17)$$

where  $C_{O_2, \text{ch}}$  is the oxygen concentration in the channel

$$C_{O_2, \text{ch}} = \frac{p_{O_2}}{RT} = 0.21 \left( \frac{p_{\text{gas}} - p_{\text{H}_2\text{O}}}{RT} \right) = 0.21 \left( \frac{p_{\text{gas}} - \text{RH} p_{\text{H}_2\text{O}}^{\text{sat}}}{RT} \right) \quad (18)$$

In this expression, RH is the relative humidity (RH = 1 was considered here) and  $p_{\text{H}_2\text{O}}^{\text{sat}}$  is the saturation pressure of water, which is a strong function of temperature [33,52]

$$\log_{10}(p_{\text{H}_2\text{O}}^{\text{sat}}) = -2.18 + 2.95 \times 10^{-2}(T - 273.15) - 9.18 \times 10^{-5}(T - 273.15)^2 + 1.44 \times 10^{-7}(T - 273.15)^3 \quad [\text{atm}] \quad (19)$$

The limiting current density provides a measure of the variations of the current density expected in PEFCs due to changes in the two-phase conditions and/or the MEA microstructure (e.g., gaps between layers due to improper assembly and fabrication defects).

### 3. Discussion of results

The discussion of results is divided into two sections. In Section 3.1, the model predictions of the baseline case ( $L_x \times L_z = 1.24 \times 1.24 \text{ mm}^2$ ,  $n_l = 2$  and  $p_c^{\text{in}} = 7.5 \text{ kPa}$ ) are compared with previous data from various literature sources in terms of: (i)  $p_c - s$  curve, (ii) effective diffusivity and (iii) IP saturation profiles. In Section 3.2, the results of a parametric analysis performed under IP conditions on the uncompressed sample are discussed. The analysis focuses on the effect of the invaded area fraction of water at the inlet and the outlet,  $A_w^{\text{in}}$  and  $A_w^{\text{out}}$ , on gas diffusion for multiple GDL samples generated stochastically ( $\sim 2000$  simulations) [29]. Specifically,  $A_w^{\text{in}}$  is varied between 0 (dry conditions) and approximately 1 (virtually fully-invaded GDL) by varying  $p_c^{\text{in}}$  between 5.75 – 11 kPa, while  $A_w^{\text{out}}$  is analyzed for three different cases by changing the representative size of the GDL domain ( $L_x \times L_z = 1.24 \times 1.24 \text{ mm}^2$  (baseline case),  $L_x \times L_z = 2.48 \times 1.24 \text{ mm}^2$  (larger domain) and  $L_x \times L_z = 0.62 \times 1.24 \text{ mm}^2$  (smaller domain)). Assuming independent water clusters in the active area, these three domain sizes correspond to different areal densities of evacuation sites from the GDL toward the channel,  $A_w^{\text{out}} = 25$  (baseline case), 12.5 and 50 droplets  $\text{cm}^{-1}$  under IP conditions (i.e., one outlet pore in the computational domain).

#### 3.1. Model comparison

Figure 3 shows the predictions for the two microscopic formulations of the capillary pressure,  $p_{c, CV}$ : (i) the Washburn equation, Eq. (2a), and (ii) the Purcell equation, Eq. (2b); see Section 2.1. The numerical results are compared with the experimental data of Gostick et al. [35] for both uncompressed (CR  $\approx 0$ ) and compressed (CR  $\approx 30\%$ ) carbon-paper samples (10 wt% PTFE Toray TGP-H 120). When

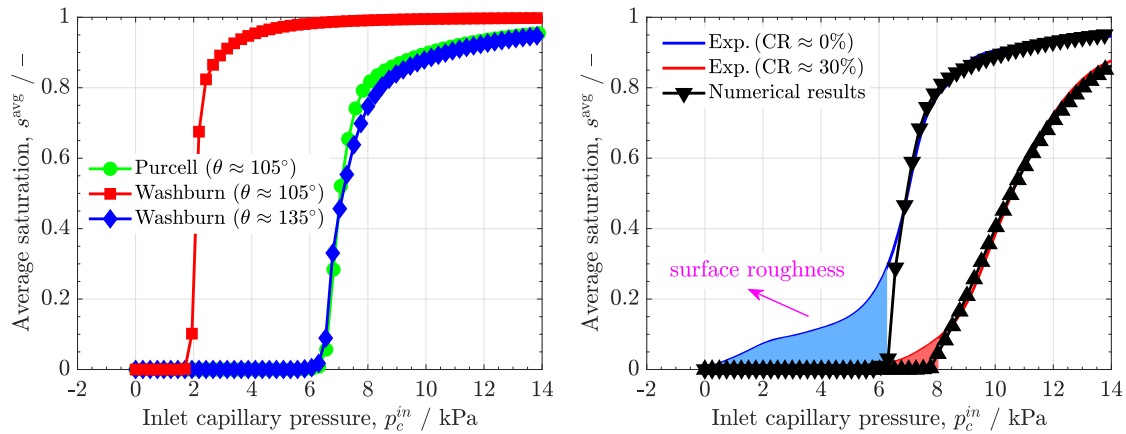


**Figure 3.** (left) Capillary pressure curve,  $p_c$ - $s$ , predicted by the hybrid model using the Purcell equation with  $\theta = 105^\circ$  and the Washburn equation with  $\theta = 105$  and  $130^\circ$ , corresponding to the uncompressed 10 wt% PTFE Toray TGP-H 120 sample. (right) Comparison between the numerical results of the hybrid model with the Purcell equation and the experimental data of Gostick et al. [35] for uncompressed and compressed (CR  $\approx$  30%) 10 wt% PTFE Toray TGP-H 120 samples.

a realistic contact angle is considered,  $\theta = 105^\circ$ , the Washburn equation (red line) leads to significantly smaller capillary pressures compared to the Purcell equation (green line). A higher contact angle,  $\theta = 130^\circ$ , is necessary with the Washburn equation (blue line) to reproduce experimental data, which is above the range of variation expected for the contact angle in mixed-wettability GDLs ( $\theta_{\text{carbon}} \approx 86^\circ$ ,  $\theta_{\text{PTFE}} \approx 108^\circ$ ) [53,54]. This result agrees with the observations of Gostick [44], confirming the good functioning of the hybrid model with the Purcell equation rather than with the Washburn equation to model capillary transport in fibrous porous media. Therefore, the microscopic Purcell formulation was used hereafter. The right panel shows that the  $p_c$ - $s$  curve of the compressed sample shifts toward higher capillary pressures due to the decrease of the average pore radius ( $r_p^{\text{unc}} \approx 15 \mu\text{m}$  vs.  $r_p^{\text{con}} \approx 11.7 \mu\text{m}$ ). Moreover, the increase of water saturation with capillary pressure is more gradual in the compressed sample, leading to an increment of the local residual gas-phase saturation and the local water-invasion resistance from  $s_{l,\text{gas}}^{r,\text{unc}} = 0.2$  to  $s_{l,\text{gas}}^{r,\text{con}} = 0.85$  and  $\eta^{\text{unc}} = 2.5$  to  $\eta^{\text{con}} = 5.75$ , respectively. This result is ascribed to the rise of internal constrictions within the pore space upon compression (see, e.g., [32,55]). The deviation between the numerical and experimental data of the uncompressed sample at low capillary pressures is explained by the surface roughness of the material, which was not explicitly taken into account in the present model [24,44]. For instance, the agreement between the numerical results and the experimental data is notably better in the compressed sample when the surface roughness is reduced [30,32,56].

Figure 4 shows the computed relative effective diffusivity,  $g_{\text{TP}}(s^{\text{avg}})$ , and the normalized effective diffusivity,  $D_{\text{TP}}^{\text{eff,wet}} D^{-1}(c_{\text{gas}}^{\text{avg}})$ , corresponding to the cases examined in Figure 3.  $g_{\text{TP}}(s^{\text{avg}})$  decreases with water saturation due to both the decrease of the pore volume available for diffusion and the increase of tortuosity. The relative effect of liquid water on gas diffusion is similar regardless of the



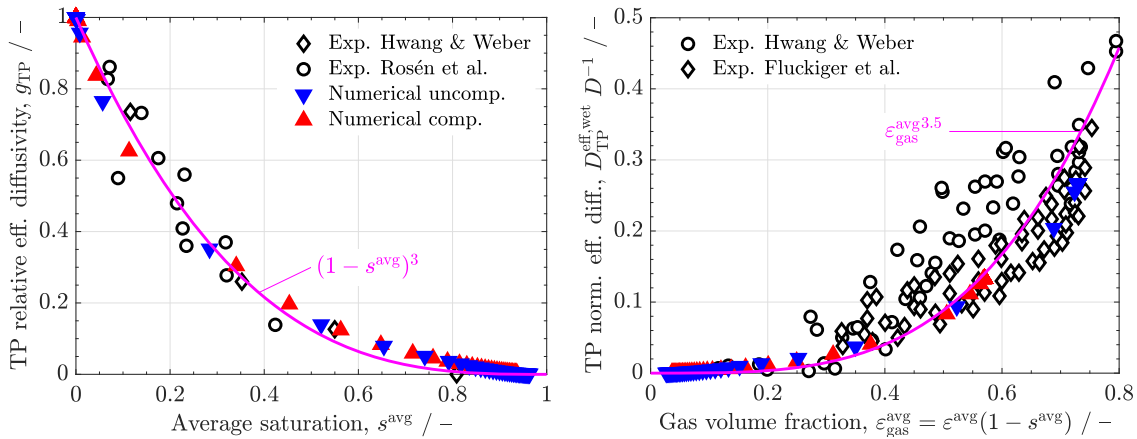


**Figure 4.** (left) TP relative effective diffusivity,  $g_{TP}$ , as a function of the average water saturation,  $s^{avg}$ , predicted by the hybrid model for the uncompressed and compressed samples. The ex-situ and in-situ experimental data of Hwang & Weber [57] and Rosén et al. [58], respectively, are included for comparison. (right) TP normalized effective diffusivity,  $D_{TP}^{eff,wet} D^{-1}$  as a function of the gas volume fraction,  $\epsilon_{gas}^{avg} = \epsilon^{avg}(1 - s^{avg})$ , predicted by the hybrid model for the uncompressed and compressed samples. The ex-situ experimental data of Hwang & Weber [57] and Flückiger et al. [60] are included for comparison. See caption to Figure 3 for further details.

compression ratio, being well correlated by a power-law relationship,  $g_{TP}(s^{avg}) \sim (1 - s^{avg})^3$ . This result agrees with the ex-situ and in-situ experimental data of Hwang & Weber [57] and Rosén et al. [58], respectively. Furthermore, the results lie in the range reported by García-Salaberri et al. [24] and Nam & Kaviany [59], who showed that the global saturation exponent in carbon-paper GDLs is typically between  $n_g \approx 3 - 4$ , depending on the finite-size arrangement of water in the sample. As a result, the local saturation exponent at the pore/throat scale,  $n_l \approx 2$ , is lower than the global saturation exponent,  $n_g \approx 3 - 4$  (see [25] for further details). The normalized effective diffusivity,  $D_{TP}^{eff,wet} D^{-1}(\epsilon_{gas}^{avg})$  increases non-linearly with the gas-phase porosity, following a power law of the form  $D_{TP}^{eff,wet} D^{-1} \sim \epsilon_{gas}^{avg,3.5}$ . A lower effective diffusivity prevails in the compressed sample under nearly dry conditions due to its lower porosity ( $f_{TP}^{dry,com} = 0.12, \epsilon^{com} = 0.57$  vs.  $f_{TP}^{dry,unc} = 0.24, \epsilon^{unc} = 0.75$ ). This result is inline with the experimental data of Hwang & Weber [57] and Flückiger et al. [60] for Toray TGP-H series with 0-20 wt% PTFE. The agreement is especially good in the case of Flückiger et al. [60] (white diamonds), whose diffusivity data are around two times lower than those reported by Hwang & Weber [57] (white circles) [29].

The through-plane saturation profiles obtained from IP simulations on ten stochastic realizations of uncompressed GDL samples are examined in Figure 5(up). The inlet capillary pressure was set equal to  $p_c^{in} = 7.5$  kPa, corresponding to an inlet saturation of  $s^{in} \approx 0.6$ . On the right panel, the mean saturation profile of the 10 samples is compared with previous PNM results [44,46,61] and ex-situ and in-situ experimental data [27,58,62]. In addition, Figure 5(down) shows an illustrative example of the species concentration distribution (continuum formulation), together with the liquid water distribution

of invaded CVs (discrete PNM formulation). In all cases, the saturation profile decreases from the injection face toward the outlet face, despite the stochastic variations among samples. This pattern arises naturally from the IP process, given that the probability of invading a throat with a low entry capillary pressure increases in regions of high specific liquid-gas interfacial area. Therefore, on average, saturation is higher near the injection face due to the larger invasion probability (higher liquid-gas interfacial area), and decreases toward the outlet face because of the descent of the invasion probability (lower liquid-gas interfacial area). The minimum saturation is inherently located at the outlet, since the IP process stops when the minimum entry capillary pressure of the invasion front is adjacent to the outlet face (i.e., one outlet pore is invaded).

As shown on the right panel, the shape of the computed mean saturation profile (black solid line) is similar to that presented in the PNM works of Gostick [44], Hinebaugh et al. [61] and Sinha et al. [46] (blue solid lines), among others. Furthermore, the results are in good agreement with the saturation profiles near the break-through point reported in the  $p_c$ - $s$  experiments of Lamibrac et al. [62] (red dashed lines), and those reported in the in-situ experiments of Rosén et al. [58] and Xu et al. [27] at low operating temperatures ( $T = 30^\circ\text{C}$  and  $T = 40^\circ\text{C}$ ). That is, in conditions where capillary fingering across the GDL is dominant rather than phase-change-induced flow (green dashed lines) [26]. The differences with the in-situ results are higher in the region facing the outlet face, since two-phase interactions with the channel and phase-change-induced flow (i.e., water evaporation/condensation [63–65]) were not taken into account in this work. Nevertheless, it is worth noting that both the PNM results and the experimental data deviate from the saturation profiles typically predicted by macro-homogeneous models, which show a curvature opposite to PNM (see, e.g. Pasaogullari & Wang [66]). As discussed by Rebai & Prat [31] and García-Salaberri et al. [30], this is explained by the lack of scale separation between the pore and layer scales in thin macro-porous media, such as GDLs, which only include a few pores in the through-plane direction [67]. The present hybrid model properly captures this aspect using the CV representation.

### 3.2. Parametric analysis (IP)

Figures 6 and 7 show the effect of the inlet invaded area fraction,  $A_w^{in}$ , on the average saturation,  $s^{avg}$ , global saturation exponent,  $n_g$ , oxygen diffusion resistance,  $R_{O_2}^{chl}$  and limiting current density,  $I_{lim}$ , corresponding to the uncompressed sample. The results are colored according to the inlet capillary pressure prescribed in the IP simulations,  $p_c^{in} = 5.75$  kPa,  $A_w^{in} \rightarrow 0$  (blue) and  $p_c^{in} = 11$  kPa,  $A_w^{in} \rightarrow 1$  (red), while the markers correspond to different local saturation exponents,  $n_l = 1.5, 2$  &  $2.5$ . Simulations were run on 10 stochastically-generated GDL samples for each  $p_c^{in}$  and  $n_l$  value.

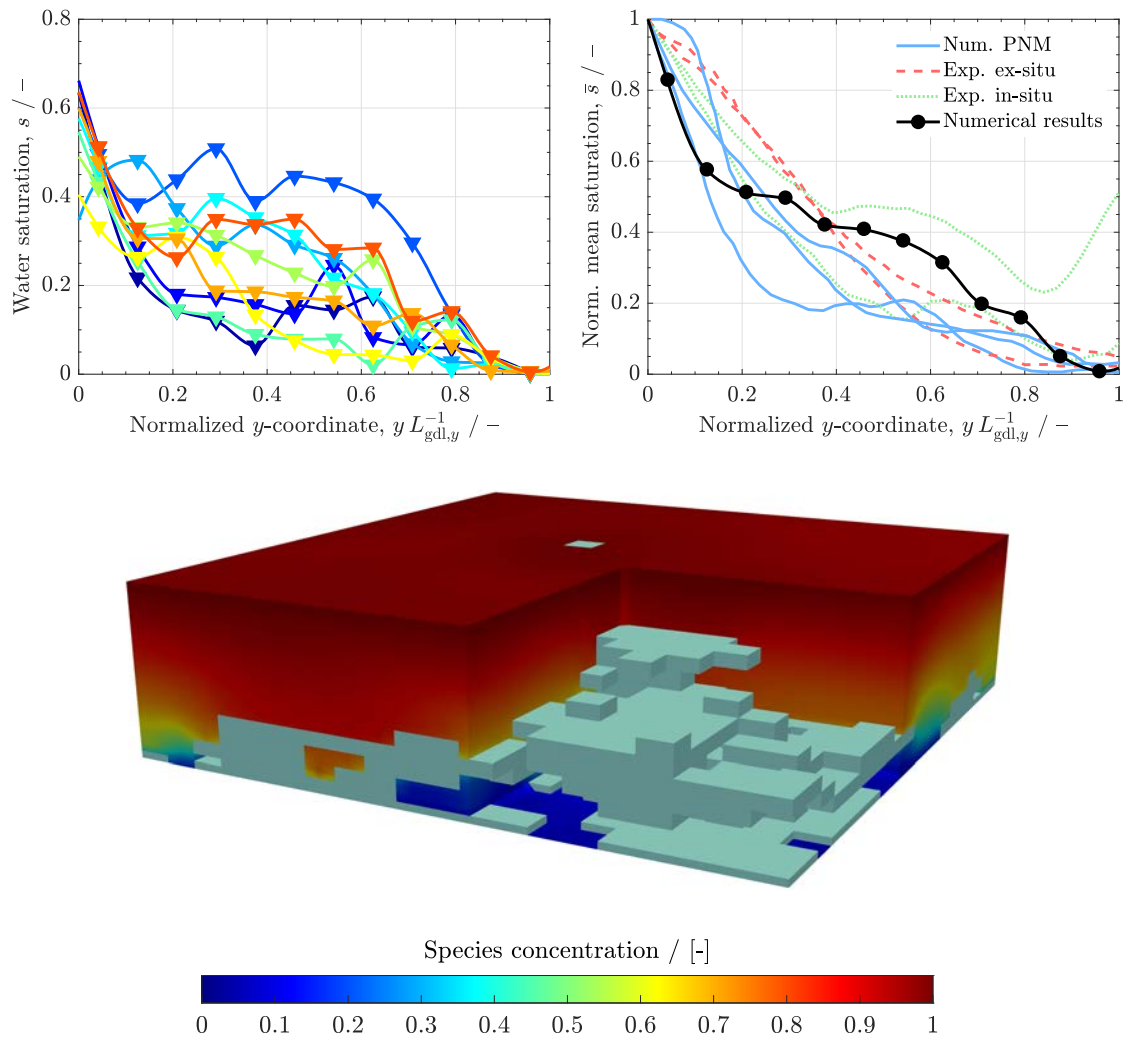


**Figure 5.** (up) TP saturation profiles,  $s(\tilde{y})$ , as a function of the normalized TP coordinate,  $\tilde{y} = y L_{\text{gd},y}^{-1}$ , predicted by the hybrid model, corresponding to IP simulations in ten stochastic realizations of uncompressed 10 wt% PTFE Toray TGP-H 120. The right plot shows the mean saturation profile of the ten samples,  $\bar{s} = s s_{\text{max}}^{-1}(\tilde{y})$ , compared with previous PNM results [44,46,61], and ex-situ [62] and in-situ [27,58] experimental data. The average profiles are normalized with respect to the maximum saturation at the inlet,  $s_{\text{max}}$ , for comparison. (down) 3D distribution of gas species concentration (continuum formulation) and liquid water (discrete PNM formulation), corresponding to an IP simulation with  $p_c^{\text{in}} = 7.5$  kPa ( $s^{\text{in}} \approx 0.6$ ). The CVs invaded by liquid water are shown in light blue.

As shown in Figure 6, when the invaded area fraction is below  $A_w^{in} \sim 0.5$ , there is a net linear increase of  $s^{avg}$  with  $A_w^{in}$  from  $s^{avg} = 0$  to  $s^{avg} \approx 0.2$  (despite the stochastic variations), so that  $s^{avg} \sim 0.4A_w^{in}$ . However, when  $A_w^{in} \gtrsim 0.5$ ,  $s^{avg}$  reaches a plateau, varying stochastically between  $s^{avg} \sim 0.1 - 0.3$ , being the mean value equal to  $s^{avg} \sim 0.2$ . Therefore, the variation of  $s^{avg}$  with  $A_w^{in}$  can be expressed as

$$s^{avg} \sim \begin{cases} 0.4A_w^{in} \pm 0.1, & 0 \lesssim A_w^{in} \lesssim 0.5 \\ 0.2 \pm 0.1, & 0.5 \lesssim A_w^{in} \lesssim 1 \end{cases} \quad (20)$$

As discussed in the Supplementary Material, this behavior is explained by the mean increase of the inlet liquid-gas interfacial area,  $A_{lg}^{in}$ , with  $s^{avg}$  in the range  $A_w^{in} \sim 0 - 0.5$  [68–70]. However, when more than half of the inlet area is invaded by water,  $A_{lg}^{in}$  reaches a maximum and then decreases moderately. Note that  $A_{lg}^{in}$  tends to the platform area of the GDL ( $A_{lg}^{in}/A_{gdl} \rightarrow 1$ ) when  $A_w^{in} \rightarrow 1$  ( $s^{in} \rightarrow 1$ ). Consequently, for  $A_w^{in} \gtrsim 0.5$ , the stochastic variations of  $s^{avg}$  overlap the mean variation of  $A_{lg}^{in}$ , leading to the plateau in  $s^{avg}$ . The range of variation of  $s^{avg}$  is in good agreement with the values typically observed in operating PEFCs between  $s^{avg} = 0.1 - 0.4$  (see, e.g., [27,58,71,72] among others).

As commented in Section 3.1, the global saturation exponent is larger than the local saturation exponent ( $n_g > n_l$ ) owing to the blockage created by the finite-size arrangement of liquid water across the GDL [24,25]. The saturation exponent remains approximately constant,  $n_g \sim 3.7$ , when the invasion of the inlet area is not exceedingly high ( $A_w^{in} \lesssim 0.5$ ). However, for higher invasion ratios,  $n_g$  moderately increases from 3.7 to 5 in the range  $0.5 \lesssim A_w^{in} \lesssim 0.8$ , and then strongly grows to more than 5 when the inlet area is highly flooded ( $A_w^{in} \gtrsim 0.8$ ). The  $n_g$  vs.  $A_w^{in}$  results can be fitted through an exponential function of the form

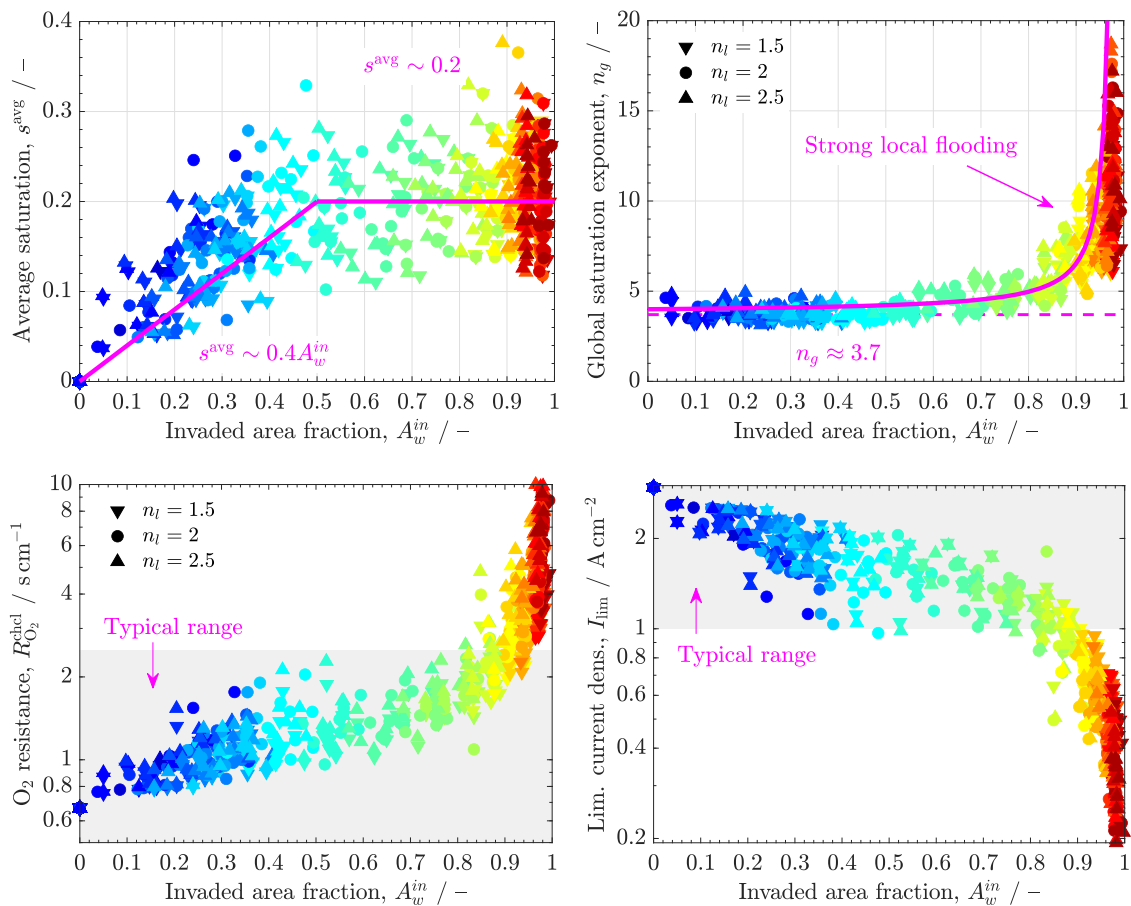
$$n_g = n_{g,o} \exp\left(\frac{\gamma A_w^{in}}{A_w^{in,th} - A_w^{in}}\right) \quad (21)$$

where  $n_{g,o}$  is the saturation exponent at low areal invasion ratios,  $A_w^{in,th}$  is the percolation threshold for which diffusion is no longer possible across the GDL, and the parameter  $\gamma$  controls the growth of  $n_g$  with  $A_w^{in}$ . The values adopted for the fitting are  $n_{g,o} = 4$ ,  $A_w^{in,th} = 0.999$  and  $\gamma = 5.4 \times 10^{-2}$ .

Therefore, the relative tortuosity originated by liquid water,  $\tau^{rel}$ , gradually increases with average saturation,  $s^{avg}$ , sharply rising toward infinity ( $n_g \rightarrow \infty$ ) when  $A_w^{in} \rightarrow 1$  (see Supplementary Material). Considering the definition of  $g(s^{avg})$  [24],  $\tau^{rel}$  can be expressed as

$$g(s^{avg}) = \frac{(1 - s^{avg})}{\tau^{rel}} = (1 - s^{avg})^{n_g} \Rightarrow \tau^{rel} = (1 - s^{avg})^{1-n_g} \quad (22)$$

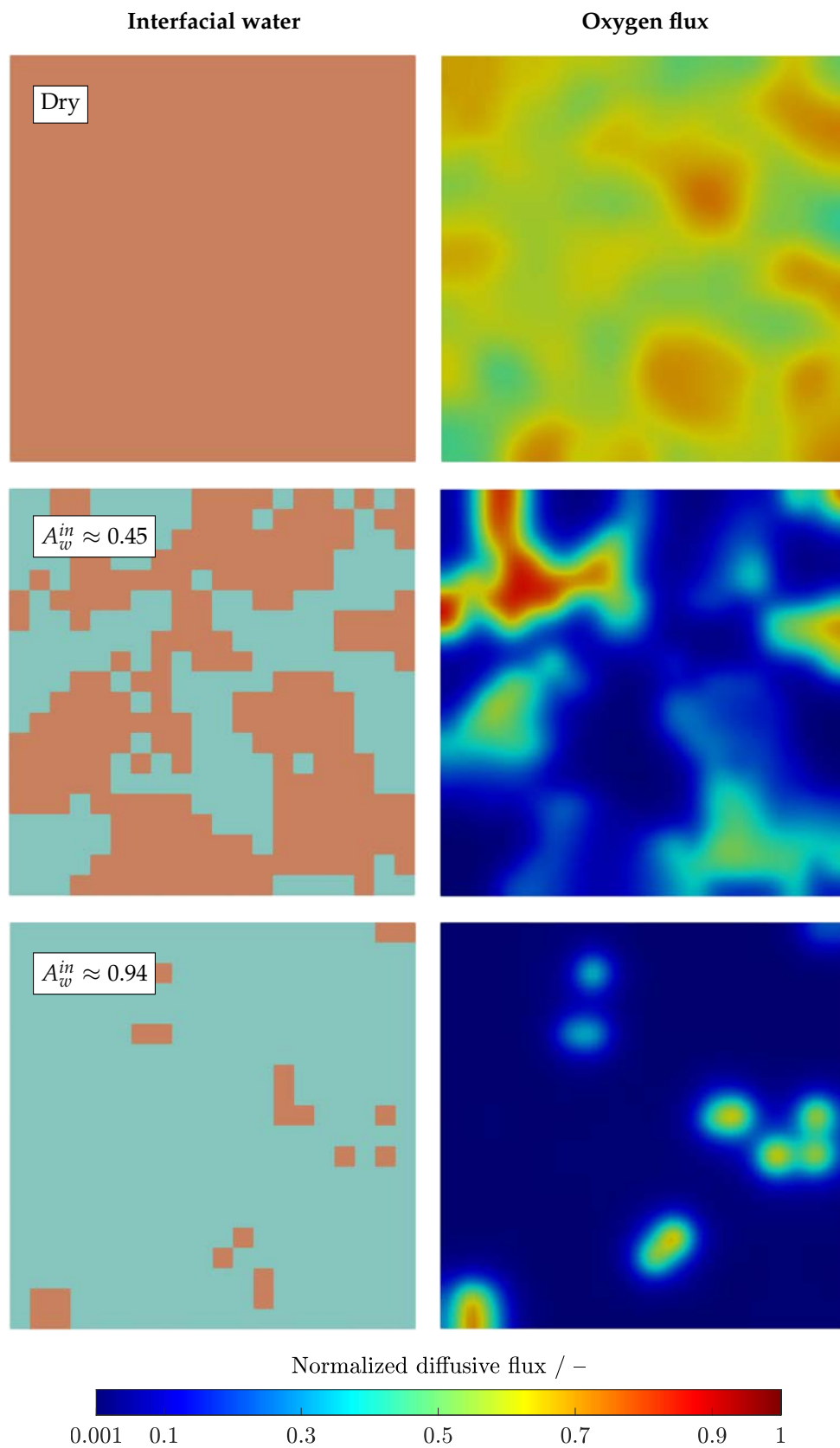
where  $s^{avg}$  and  $n_g$  are given by Eqs. (20)-(21), respectively.



**Figure 6.** Variation of the average saturation,  $s^{avg}$ , global saturation exponent,  $n_g$ , oxygen diffusion resistance,  $R_{O_2}^{chl}$ , and limiting current density,  $I_{lim}$ , as a function of the invaded area fraction,  $A_w^{in}$ , corresponding to three different local saturation exponents:  $n_l = 1.5$  (downward triangles),  $n_l = 2$  (circles) and  $n_l = 2.5$  (upward triangles). The data are colored according to the inlet capillary pressure prescribed in the IP simulations from blue ( $p_c^{in} = 5.75$  kPa,  $A_w^{in} \rightarrow 0$ ) to red ( $p_c^{in} = 11$  kPa,  $A_w^{in} \rightarrow 1$ ). The fits to the  $s^{avg}$  and  $n_g$  results are also included (see Eqs. (20)-(21)).

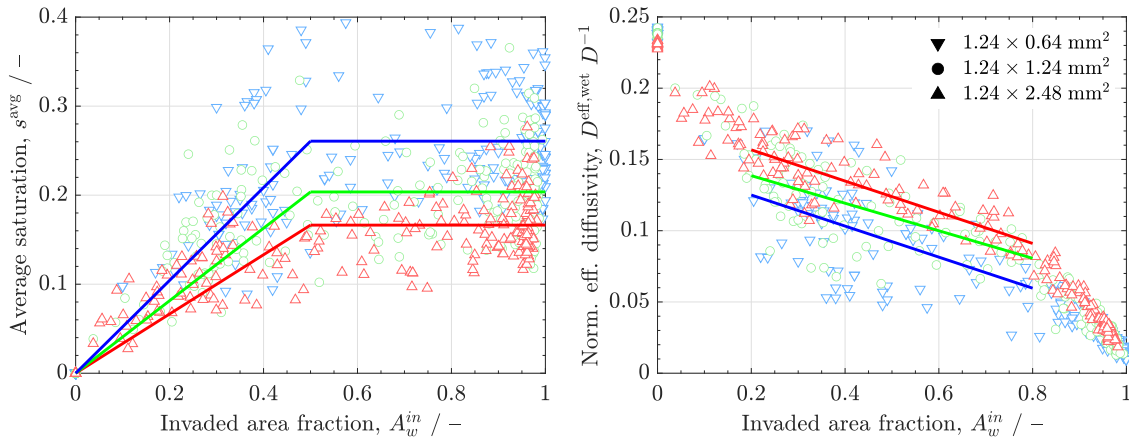
The above results clearly show that low interfacial water saturations facilitate gas diffusion in PEFCs, as it is usually found in practice when an MPL is added in the face adjacent to the CL [35,73]. Local flooding is catastrophic for species diffusion, as shown in the experiments of Koresawa & Utaka [74], who reported saturation exponents as high as  $n_g \approx 7 - 9$  [24] due to the presence of a high saturation region near their inlet pipe (i.e., highly flooded gap). In an operating PEFC, this situation can also often arise (see, e.g., Kundu et al. [75], Simon et al. [76] and Qin et al. [77]) because of the existence of interfacial gaps between layered components. Possible causes are the presence of gaps between the CL and the MPL at low compressions, the absence of an MPL or gaps due to the delamination of components with time. This undesirable scenario can lead to local reactant starvation, and eventually can result in a dramatic decrease of the cell performance at high current densities due to large concentration losses [76]. Moreover, local flooding can affect durability, e.g., corrosion of the carbon support in the cathode CL because of hydrogen starvation at the anode [78,79]. Quantitatively, the oxygen diffusion resistance increases continuously between  $R_{O_2}^{\text{chl}} \sim 1 - 2 \text{ s cm}^{-1}$  when  $A_w^{\text{in}} \approx 0 - 0.8$ , strongly rising up to  $R_{O_2}^{\text{chl}} \sim 10 \text{ s cm}^{-1}$  for  $A_w^{\text{in}} \gtrsim 0.8$ . The continuous increase of  $R_{O_2}^{\text{chl}}$  is explained by the growth of both  $s^{\text{avg}}$  and  $\tau^{\text{rel}}$  with  $A_w^{\text{in}}$ . As a result, the limiting current density decreases from  $I_{\text{lim}} \sim 2.5 \text{ A cm}^{-2}$  to  $I_{\text{lim}} \sim 1 \text{ A cm}^{-2}$  in the range  $A_w^{\text{in}} \approx 0.2 - 0.8$ , and drops sharply toward  $I_{\text{lim}} \rightarrow 0$  for  $A_w^{\text{in}} \gtrsim 0.8$ . Similar variations to those observed here at  $A_w^{\text{in}} \approx 0.2 - 0.9$  ( $R_{O_2}^{\text{chl}} \approx 1 - 3 \text{ s cm}^{-1}$ ,  $I_{\text{lim}} \approx 2.5 - 1 \text{ A cm}^{-2}$ ) were reported in previous in-situ experimental studies (see, e.g., [19,24,25,76]), with  $R_{O_2}^{\text{chl}} \approx 1 - 2.5 \text{ s cm}^{-1}$  at  $I_{\text{lim}} \approx 1 - 3 \text{ A cm}^{-2}$ .

Figure 7 shows the spatial distributions of the inlet interfacial water (i.e., inlet invaded CVs) and the corresponding normalized oxygen diffusive flux,  $j_y j_{y,\text{max}}^{-1}$ , for three different area ratios,  $A_w^{\text{in}} = 0$  (dry), 0.45 & 0.94. The same colorbar is used in the three plots for comparison purposes. The impact of the dry microstructure of the GDL on diffusion is not negligible, leading to variations of one order of magnitude. Similar numerical results were recently presented by García-Salaberri et al. [29,80] and Hack et al. [81]. The effect of liquid water in the partially-saturated samples is superimposed to that of the microstructure, amplifying the differences. The diffusive flux varies up to 3-4 orders of magnitude, owing to the vanishing local flux in the flooded regions of the GDL. This result highlights the importance of the multiscale nature of flooding, since local flooded regions (zero flux) are present within partially-saturated samples. This fact can usually be neglected for averaged quantities over the entire active area (e.g., average current density), where the mean is essentially given by the sum of the contribution of representative samples (with certain effective properties). However, the same does not necessarily hold for local degradation processes, given that local reactant starvation can affect the degradation of neighboring areas within a representative sample, which, in turn, can affect the degradation of neighboring representative samples. This fundamental aspect warrants further



**Figure 7.** Spatial distributions of interfacial water (invaded CVs) and normalized oxygen diffusive flux,  $\tilde{j} = j_y j_{y,\max}^{-1}$ , at the inlet, corresponding to three different invaded area fractions,  $A_w^{in} = 0$  (dry), 0.45 & 0.94.





**Figure 8.** Variation of (left) the average saturation,  $s^{\text{avg}}$ , and (right) the TP normalized effective diffusivity,  $D_{\text{TP}}^{\text{eff,wet}} D^{-1}$ , as a function of the invaded area fraction,  $A_w^{\text{in}}$ , corresponding to three different domain sizes:  $1.24 \times 0.64 \text{ mm}^2$  (downward triangles),  $1.24 \times 1.24 \text{ mm}^2$  (circles) and  $1.24 \times 2.48 \text{ mm}^2$  (upward triangles). These three cases correspond to different areal densities of water evacuation sites toward the channel,  $A_w^{\text{out}} = 50, 25$  and  $12.5$  droplets  $\text{cm}^{-1}$ , respectively.

attention and could be examined with the hybrid model considering different resolutions in the material plane.

The results of the analysis of the evacuation area fraction at the outlet,  $A_w^{\text{out}}$ , on the uncompressed sample are shown in Figure 8. The left and the right panels show the variation of the average saturation,  $s^{\text{avg}}$ , and the normalized effective diffusivity,  $D_{\text{TP}}^{\text{eff,wet}} D^{-1}$ , as a function of the invaded area fraction at the inlet,  $A_w^{\text{in}}$ , respectively. The results of the three outlet water fractions (representative domain sizes) are colored in red,  $A_w^{\text{out}} = 12.5$  droplets  $\text{cm}^{-1}$  ( $L_x \times L_z = 2.48 \times 1.24 \text{ mm}^2$ ), green,  $A_w^{\text{out}} = 25$  droplets  $\text{cm}^{-1}$  ( $L_x \times L_z = 1.24 \times 1.24 \text{ mm}^2$ ), and blue,  $A_w^{\text{out}} = 50$  droplets  $\text{cm}^{-1}$  ( $L_x \times L_z = 0.62 \times 1.24 \text{ mm}^2$ ). The markers correspond to the three local saturation exponents,  $n_l = 1.5, 2$  &  $2.5$ . The amount of water gradually increases with the areal fraction of evacuation sites from the GDL toward the channel (smaller domain size), with a similar effect of  $A_w^{\text{in}}$  to that discussed before in Figure 6. In all the cases, the mean value of  $s^{\text{avg}}$  increases almost linearly with  $A_w^{\text{in}}$ , reaching a plateau for  $A_w^{\text{in}} \gtrsim 0.5$ . The stochastic variations of  $s^{\text{avg}}$  around the mean value amount up to  $\Delta s^{\text{avg}} \sim 0.1 - 0.15$ . Therefore, the piecewise dependence of  $s_{\text{avg}}$  on  $A_w^{\text{in}}$  corresponding to the three domain sizes can be expressed as

$$s^{\text{avg}}(50/25/12.5 \text{ droplets cm}^{-1}) \sim \begin{cases} 0.52/0.4/0.33 A_w^{\text{in}} \pm 0.1, & 0 \lesssim A_w^{\text{in}} \lesssim 0.5 \\ 0.26/0.2/0.17 \pm 0.15, & 0.5 \lesssim A_w^{\text{in}} \lesssim 1 \end{cases} \quad (23)$$

where the value between brackets indicate the areal density of droplets (12.5 – 50 droplets  $\text{cm}^{-1}$ ).

Consequently, there is a net decrease of  $D_{\text{TP}}^{\text{eff,wet}} D^{-1}$  as the number of evacuation sites is higher due to the larger water saturations reached in the GDL. The differences are small under nearly dry

conditions ( $A_w^{in} \rightarrow 0$ ) or when the invasion area is close to the percolation threshold ( $A_w^{in} \rightarrow 1$ ), while they are more significant in the intermediate range between  $0.2 \lesssim A_w^{in} \lesssim 0.8$ . This range of invaded area fractions is expected to be more frequently found in practice. The variation of the mean value of  $D_{TP}^{eff,wet} D^{-1}$  with  $A_w^{in}$  is almost linear in the range of interest, with a similar slope but different intercept for the three cases under study, i.e.,

$$D_{TP}^{eff,wet} D^{-1} \sim \begin{cases} 0.15 - 0.11A_w^{in}, & 50 \text{ droplets cm}^{-1} \\ 0.16 - 0.1A_w^{in}, & 25 \text{ droplets cm}^{-1} \\ 0.18 - 0.11A_w^{in}, & 12.5 \text{ droplets cm}^{-1} \end{cases} \quad (24)$$

The above results show the importance of an appropriate design of the GDL/MPL to reduce the number of evacuation sites of water and facilitate gas diffusion. In an operating PEMFC, the rise of the number of evacuation sites is inherently coupled to the increase of the current density, aggravating concentration losses [15,82]. The use of MPLs has been shown to be an effective solution to decrease the number of invading clusters into the GDL and in turn reduce the number of breakthrough locations (see, e.g., [83,84]). However, the optimal MPL/GDL design is still a source of research. Key aspects that deserve further attention are the spacing (i.e., areal density) of cracks in the MPL, GDL microstructure (e.g., ordered microstructures), MPL intrusion into the GDL, wettability and water interactions with the channel [15,49,83,85–87]. An optimal GDL/MPL should provide patterned paths for liquid water and gas diffusion and low water spreading inside the GDL (i.e., providing narrow straight paths for water) over a wide range of operating temperatures.

#### 4. Conclusions

A hybrid formulation has been presented to examine the interplay between gas diffusion and water capillary transport in gas diffusion layers (GDLs) used in proton exchange fuel cells (PEFCs). The model divides the GDL into a control volume (CV) mesh, which embeds a structured pore network (PN) representation of the pore space. Here, one pore (with six throats) was included in each CV, even though several pores per CV could also be taken into account. The PN geometry was used to determine: (i) local anisotropic effective diffusivities and (ii) entry/characteristic capillary pressures and local saturations in each CV. This information was easily incorporated into a CFD code (ANSYS Fluent) to model gas diffusion using a continuum formulation and to model water capillary transport using a discrete formulation. Capillary pressure curves and invasion-percolation (IP) were simulated by treating CVs as pore bodies and faces between CVs as connecting throats. Computational meshes with 27 numerical cells were included in each CV to accurately capture the blockage of liquid water on gas diffusion, while keeping computational cost moderate (less than 30 s per case).

The model was validated with several numerical and experimental literature sources considering an uncompressed and a 30% compressed carbon-paper GDL (Toray TGP-H). The variables selected for comparison were: (i) capillary pressure curve,  $p_c-s$ , (ii) relative effective diffusivity,  $g_{g,y}$ , and normalized effective diffusivity,  $D^{\text{eff,wet}} D^{-1}$ , and (iii) through-plane saturation profile,  $s(y)$ . The analysis showed that the Purcell toroid formulation provides a better description of local capillary transport in fibrous materials compared to the Washburn equation. The capillary pressure was larger and the water uptake was more gradual in the compressed sample due to its lower characteristic pore radius and the more complex microstructure that arise from compression. However, no significant changes were observed in the relative effective diffusivity with compression, being well described through a power law of the form  $g_{g,y} = (1 - s)^n$ , with global and local saturation exponents equal to  $n_l \approx 2$  and  $n_g \approx 3$ , respectively. The saturation profiles from IP simulations showed an opposite curvature to the predictions of macro-homogenous continuum models, which was explained by the lack of separation between pore and layer scales in thin GDLs. The computed profiles were similar to those found in operating PEFCs at low temperature (30 – 40 °C), with water saturation gradually decreasing from the CL toward the channel.

Subsequently, the effect of the invaded area fraction at the inlet and the outlet,  $A_w^{\text{in}}$  and  $A_w^{\text{out}}$ , respectively, on several variables of interest, was examined, including: (i) average saturation,  $s^{\text{avg}}$ , (ii) oxygen diffusion resistance,  $R_{\text{O}_2,\text{chcl}}$ , and (iii) limiting current density,  $I_{\text{lim}}$ , among others. The results showed that gas diffusion in GDLs cannot be described by average saturation alone, owing to the impact of the finite-size arrangement of water. On average, the increase of  $n_g$  is small when  $A_w^{\text{in}} \lesssim 0.5$ , but increases exponentially when  $A_w^{\text{in}} \gtrsim 0.5$ , eventually leading to strong blockage of gas diffusion for  $A_w^{\text{in}} \gtrsim 0.8$  due to local flooding near the inlet region. This situation can arise in operating PEFCs by the presence of bottlenecks created by flooded interfacial gaps and defects between the GDL/MPL and the catalyst layer, resulting in a dramatic increase of the oxygen diffusion resistance (i.e., decrease of the limiting current density). The analysis of  $A_w^{\text{out}}$  (i.e., the number of evacuation sites toward the channel) revealed that the gas effective diffusivity decreases with the number of independent water clusters over the cell active area (i.e., an increment of  $A_w^{\text{out}}$ ). This is explained by the overall increase of average saturation with  $A_w^{\text{out}}$ , which reaches  $s^{\text{avg}} = 0.26, 0.2$  &  $0.17$  for  $A_w^{\text{out}} = 25, 12.5$  &  $50$  droplets  $\text{cm}^{-1}$ , respectively. These results highlight the importance of optimizing interfacial transport of water through the layered components of the MEA for adequate water management in high-performance PEFCs.

Several aspects warrant further attention. Future model developments should consider the incorporation of phase-change phenomena and other layers of the MEA (MPL and catalyst layer) in the hybrid formulation, along with GDL/channel interactions. In addition, the hybrid model can be used to derive improved fully macroscopic formulations, which can overcome discrepancies existing

between macro-homogeneous models and experimental data. These advancements will allow a better understanding of water transport in multiscale layered porous media for the design of optimized MEAs, and an analysis of the effect of water flooding on durability at multiple length scales.

**Funding:** This work was supported by the projects PID2019-106740RB-I00 and EIN2020-112247 (Spanish Agencia Estatal de Investigación) and the project PEM4ENERGY-CM-UC3M funded by the call “Programa de apoyo a la realización de proyectos interdisciplinares de I+D para jóvenes investigadores de la Universidad Carlos III de Madrid 2019-2020” under the frame of the “Convenio Plurianual Comunidad de Madrid-Universidad Carlos III de Madrid”. Mr. D. Zapardiel also acknowledges the support of the excellence scholarship from the Comunidad de Madrid.

**Conflicts of Interest:** The authors declare no conflict of interest.

## Nomenclature

$A$	area / $\text{m}^2$
$C$	molar concentration / $\text{mol m}^{-3}$
$Ca$	capillary number / –
CR	compression ratio / –
$D$	bulk mass diffusivity / $\text{m}^2 \text{s}^{-1}$
$\overline{\overline{D}}^{\text{eff}}$	effective diffusivity tensor / $\text{m}^2 \text{s}^{-1}$
$d_f$	fiber diameter / m
$F$	Faraday's constant / $\text{C mol}^{-1}$
$f_r$	PSD fraction / –
$f(\varepsilon)$	normalized dry effective diffusivity / –
$g(s)$	relative effective diffusivity / –
$H$	half-height / m
$I$	current density / $\text{A m}^{-2}$
IP	invasion-percolation / –
$j_i$	diffusive flux in $i$ -direction / $\text{mol m}^{-2} \text{s}^{-1}$
$L$	length / m
$M$	viscosity ratio / –
$N$	number of control volumes in GDL / –
$n$	saturation exponent / –
$p$	pressure / Pa
$p_c$	capillary pressure / Pa
PSD	pore size distribution / $\text{m}^{-1}$
$R$	universal gas constant / $\text{J mol}^{-1} \text{K}^{-1}$
$R_i$	diffusion resistance / $\text{s m}^{-1}$
RH	relative humidity / –
$r$	radius / m
$r_0$	PSD characteristic radius / m
$s$	liquid water saturation / –
$T$	temperature / K
$t$	time / s
$V$	volume / $\text{m}^3$
$W$	half-width / m
$x$	$x$ -coordinate in the material plane / m
$y$	$y$ -coordinate through the thickness / m
$z$	$z$ -coordinate in the material plane / m

***Greek letters***

$\alpha$	angle beyond the apex of curved throat / °
$\beta$	number of computational cells per CV / –
$\Gamma$	size scaling parameter / –
$\gamma$	fitting parameter in Eq. (21)
$\delta$	thickness / m
$\varepsilon$	porosity or volume fraction / –
$\eta$	water invasion parameter / –
$\theta$	contact angle / °
$\sigma$	PSD standard deviation / m or surface tension / $\text{Nm}^{-1}$
$\tau$	tortuosity / –

***Subscripts***

CV	control volume
<i>c</i>	characteristic
ch	channel
cl	catalyst layer
<i>cp</i>	computational
<i>g</i>	global property
gas	gas phase
gdl	gas diffusion layer
<i>l</i>	local property
<i>lg</i>	liquid-gas interface
lim	limiting
max	maximum
min	minimum
mpl	micro-porous layer
<i>p</i>	pore
res	reservoir
<i>t</i>	throat
TP	through-plane direction
<i>th</i>	percolation threshold
<i>w</i>	water

***Superscripts***

<i>avg</i>	average
<i>com</i>	compressed
<i>chcl</i>	channel-catalyst layer
<i>dry</i>	dry conditions
<i>e</i>	entry condition
<i>eff</i>	effective
<i>in</i>	inlet
<i>out</i>	outlet
<i>r</i>	residual
<i>rel</i>	relative
<i>sat</i>	saturated conditions
<i>unc</i>	uncompressed
<i>wet</i>	wet conditions



## References

1. Wee, J.H. Applications of proton exchange membrane fuel cell systems. *Renewable and sustainable energy reviews* **2007**, *11*, 1720–1738.
2. Yoshida, T.; Kojima, K. Toyota MIRAI fuel cell vehicle and progress toward a future hydrogen society. *The Electrochemical Society Interface* **2015**, *24*, 45.
3. Costamagna, P.; Srinivasan, S. Quantum jumps in the PEMFC science and technology from the 1960s to the year 2000: Part II. Engineering, technology development and application aspects. *Journal of power sources* **2001**, *102*, 253–269.
4. Xu, Z.; Qiu, D.; Yi, P.; Peng, L.; Lai, X. Towards mass applications: A review on the challenges and developments in metallic bipolar plates for PEMFC. *Progress in Natural Science: Materials International* **2020**.
5. Wang, G.; Yu, Y.; Liu, H.; Gong, C.; Wen, S.; Wang, X.; Tu, Z. Progress on design and development of polymer electrolyte membrane fuel cell systems for vehicle applications: A review. *Fuel Processing Technology* **2018**, *179*, 203–228.
6. Yue, M.; Jemei, S.; Zerhouni, N.; Gouriveau, R. Proton exchange membrane fuel cell system prognostics and decision-making: Current status and perspectives. *Renewable Energy* **2021**.
7. Kurtz, J.M.; Sprik, S.; Saur, G.; Onorato, S. Fuel cell electric vehicle durability and fuel cell performance. Technical report, National Renewable Energy Lab.(NREL), Golden, CO (United States), 2019.
8. Jiao, K.; Xuan, J.; Du, Q.; Bao, Z.; Xie, B.; Wang, B.; Zhao, Y.; Fan, L.; Wang, H.; Hou, Z.; others. Designing the next generation of proton-exchange membrane fuel cells. *Nature* **2021**, *595*, 361–369.
9. Cullen, D.A.; Neyerlin, K.C.; Ahluwalia, R.K.; Mukundan, R.; More, K.L.; Borup, R.L.; Weber, A.Z.; Myers, D.J.; Kusoglu, A. New roads and challenges for fuel cells in heavy-duty transportation. *Nature energy* **2021**, *6*, 462–474.
10. Al-Othman, A.; Tremblay, A.Y.; Pell, W.; Liu, Y.; Peppley, B.A.; Ternan, M. The effect of glycerol on the conductivity of Nafion-free ZrP/PTFE composite membrane electrolytes for direct hydrocarbon fuel cells. *Journal of Power Sources* **2012**, *199*, 14–21.
11. Al-Othman, A.; Nancarrow, P.; Tawalbeh, M.; Ka'ki, A.; El-Ahwal, K.; El Taher, B.; Alkasrawi, M. Novel composite membrane based on zirconium phosphate-ionic liquids for high temperature PEM fuel cells. *International Journal of Hydrogen Energy* **2021**, *46*, 6100–6109.
12. Jiao, K.; Li, X. Water transport in polymer electrolyte membrane fuel cells. *Progress in energy and combustion Science* **2011**, *37*, 221–291.
13. Deng, X.; Zhang, J.; Fan, Z.; Tan, W.; Yang, G.; Wang, W.; Zhou, W.; Shao, Z. Understanding and engineering of multiphase transport processes in membrane electrode assembly of proton-exchange membrane fuel cells with a focus on the cathode catalyst layer: a review. *Energy & Fuels* **2020**, *34*, 9175–9188.
14. Niblett, D.; Niasar, V.; Holmes, S. Enhancing the performance of fuel cell gas diffusion layers using ordered microstructural design. *Journal of The Electrochemical Society* **2019**, *167*, 013520.
15. Niblett, D.; Mularczyk, A.; Niasar, V.; Eller, J.; Holmes, S. Two-phase flow dynamics in a gas diffusion layer-gas channel-microporous layer system. *Journal of Power Sources* **2020**, *471*, 228427.
16. Shrestha, P.; Ouellette, D.; Lee, J.; Ge, N.; Wong, A.K.C.; Muirhead, D.; Liu, H.; Banerjee, R.; Bazylak, A. Graded Microporous Layers for Enhanced Capillary-Driven Liquid Water Removal in Polymer Electrolyte Membrane Fuel Cells. *Advanced Materials Interfaces* **2019**, *6*, 1901157.
17. Qi, M.; Zeng, Y.; Hou, M.; Gou, Y.; Song, W.; Chen, H.; Wu, G.; Jia, Z.; Gao, Y.; Zhang, H.; others. Free-standing and ionomer-free 3D platinum nanotrough fiber network electrode for proton exchange membrane fuel cells. *Applied Catalysis B: Environmental* **2021**, *298*, 120504.
18. Kusoglu, A.; Vezzù, K.; Hegde, G.A.; Nawn, G.; Motz, A.R.; Sarode, H.N.; Haugen, G.M.; Yang, Y.; Seifert, S.; Yandrasits, M.A.; others. Transport and morphology of a proton exchange membrane based on a doubly functionalized perfluorosulfonic imide side chain perfluorinated polymer. *Chemistry of Materials* **2019**, *32*, 38–59.
19. Owejan, J.P.; Owejan, J.E.; Gu, W. Impact of platinum loading and catalyst layer structure on PEMFC performance. *Journal of The Electrochemical Society* **2013**, *160*, F824.
20. Fan, J.; Chen, M.; Zhao, Z.; Zhang, Z.; Ye, S.; Xu, S.; Wang, H.; Li, H. Bridging the gap between highly active oxygen reduction reaction catalysts and effective catalyst layers for proton exchange membrane fuel cells. *Nature Energy* **2021**, *6*, 475–486.

21. Weber, A.Z.; Borup, R.L.; Darling, R.M.; Das, P.K.; Dursch, T.J.; Gu, W.; Harvey, D.; Kusoglu, A.; Litster, S.; Mench, M.M.; others. A critical review of modeling transport phenomena in polymer-electrolyte fuel cells. *Journal of The Electrochemical Society* **2014**, *161*, F1254.
22. Jahnke, T.; Futter, G.; Latz, A.; Malkow, T.; Papakonstantinou, G.; Tsotridis, G.; Schott, P.; Gérard, M.; Quinaud, M.; Quiroga, M.; others. Performance and degradation of Proton Exchange Membrane Fuel Cells: State of the art in modeling from atomistic to system scale. *Journal of Power Sources* **2016**, *304*, 207–233.
23. Zenyuk, I.V.; Parkinson, D.Y.; Hwang, G.; Weber, A.Z. Probing water distribution in compressed fuel-cell gas-diffusion layers using X-ray computed tomography. *Electrochemistry Communications* **2015**, *53*, 24–28.
24. García-Salaberri, P.A.; Hwang, G.; Vera, M.; Weber, A.Z.; Gostick, J.T. Effective diffusivity in partially-saturated carbon-fiber gas diffusion layers: Effect of through-plane saturation distribution. *International Journal of Heat and Mass Transfer* **2015**, *86*, 319–333.
25. García-Salaberri, P.A.; Gostick, J.T.; Hwang, G.; Weber, A.Z.; Vera, M. Effective diffusivity in partially-saturated carbon-fiber gas diffusion layers: Effect of local saturation and application to macroscopic continuum models. *Journal of Power Sources* **2015**, *296*, 440–453.
26. Carrere, P.; Prat, M. Liquid water in cathode gas diffusion layers of PEM fuel cells: Identification of various pore filling regimes from pore network simulations. *International Journal of Heat and Mass Transfer* **2019**, *129*, 1043–1056.
27. Xu, H.; Nagashima, S.; Nguyen, H.P.; Kishita, K.; Marone, F.; Büchi, F.N.; Eller, J. Temperature dependent water transport mechanism in gas diffusion layers revealed by subsecond operando X-ray tomographic microscopy. *Journal of Power Sources* **2021**, *490*, 229492.
28. Chen, L.; Kang, Q.; Tao, W. Pore-scale numerical study of multiphase reactive transport processes in cathode catalyst layers of proton exchange membrane fuel cells. *International Journal of Hydrogen Energy* **2021**, *46*, 13283–13297.
29. García-Salaberri, P. Modeling diffusion and convection in thin porous transport layers using a composite continuum-network model: Application to gas diffusion layers in polymer electrolyte fuel cells. *International Journal of Heat and Mass Transfer* **2021**, *167*, 120824.
30. García-Salaberri, P.A.; Zenyuk, I.V.; Shum, A.D.; Hwang, G.; Vera, M.; Weber, A.Z.; Gostick, J.T. Analysis of representative elementary volume and through-plane regional characteristics of carbon-fiber papers: diffusivity, permeability and electrical/thermal conductivity. *International Journal of Heat and Mass Transfer* **2018**, *127*, 687–703.
31. Rebai, M.; Prat, M. Scale effect and two-phase flow in a thin hydrophobic porous layer. Application to water transport in gas diffusion layers of proton exchange membrane fuel cells. *Journal of Power Sources* **2009**, *192*, 534–543.
32. Zenyuk, I.V.; Parkinson, D.Y.; Connolly, L.G.; Weber, A.Z. Gas-diffusion-layer structural properties under compression via X-ray tomography. *Journal of Power Sources* **2016**, *328*, 364–376.
33. García-Salaberri, P.; Sánchez, D.; Boillat, P.; Vera, M.; Friedrich, K.A. Hydration and dehydration cycles in polymer electrolyte fuel cells operated with wet anode and dry cathode feed: A neutron imaging and modeling study. *Journal of power sources* **2017**, *359*, 634–655.
34. Liu, J.; García-Salaberri, P.A.; Zenyuk, I.V. Bridging scales to model reactive diffusive transport in porous media. *Journal of The Electrochemical Society* **2019**, *167*, 013524.
35. Gostick, J.T.; Ioannidis, M.A.; Fowler, M.W.; Pritzker, M.D. Wettability and capillary behavior of fibrous gas diffusion media for polymer electrolyte membrane fuel cells. *Journal of Power Sources* **2009**, *194*, 433–444.
36. Gostick, J.T.; Ioannidis, M.A.; Fowler, M.W.; Pritzker, M.D. Characterization of the capillary properties of gas diffusion media. In *Modeling and diagnostics of polymer electrolyte fuel cells*; Springer, 2009; pp. 225–254.
37. Chan, C.; Zamel, N.; Li, X.; Shen, J. Experimental measurement of effective diffusion coefficient of gas diffusion layer/microporous layer in PEM fuel cells. *Electrochimica Acta* **2012**, *65*, 13–21.
38. Andisheh-Tadbir, M.; El Hannach, M.; Kjeang, E.; Bahrami, M. An analytical relationship for calculating the effective diffusivity of micro-porous layers. *international journal of hydrogen energy* **2015**, *40*, 10242–10250.
39. Lee, J.; Yip, R.; Antonacci, P.; Ge, N.; Kotaka, T.; Tabuchi, Y.; Bazylak, A. Synchrotron investigation of microporous layer thickness on liquid water distribution in a PEM fuel cell. *Journal of The Electrochemical Society* **2015**, *162*, F669.
40. Fishman, Z.; Bazylak, A. Heterogeneous through-plane porosity distributions for treated PEMFC GDLs. II. Effect of MPL cracks. *Journal of The Electrochemical Society* **2011**, *158*, B846.

41. Gostick, J.T.; Fowler, M.W.; Pritzker, M.D.; Ioannidis, M.A.; Behra, L.M. In-plane and through-plane gas permeability of carbon fiber electrode backing layers. *Journal of Power Sources* **2006**, *162*, 228–238.
42. El-Kharouf, A.; Mason, T.J.; Brett, D.J.; Pollet, B.G. Ex-situ characterisation of gas diffusion layers for proton exchange membrane fuel cells. *Journal of Power Sources* **2012**, *218*, 393–404.
43. Rashapov, R.R.; Unno, J.; Gostick, J.T. Characterization of PEMFC gas diffusion layer porosity. *Journal of The Electrochemical Society* **2015**, *162*, F603.
44. Gostick, J.T. Random pore network modeling of fibrous PEMFC gas diffusion media using Voronoi and Delaunay tessellations. *Journal of the Electrochemical Society* **2013**, *160*, F731.
45. Lenormand, R.; Touboul, E.; Zarcone, C. Numerical models and experiments on immiscible displacements in porous media. *Journal of fluid mechanics* **1988**, *189*, 165–187.
46. Sinha, P.K.; Mukherjee, P.P.; Wang, C.Y. Impact of GDL structure and wettability on water management in polymer electrolyte fuel cells. *Journal of Materials Chemistry* **2007**, *17*, 3089–3103.
47. Mason, G.; Morrow, N.R. Effect of contact angle on capillary displacement curvatures in pore throats formed by spheres. *Journal of colloid and interface science* **1994**, *168*, 130–141.
48. Mularczyk, A.; Lin, Q.; Niblett, D.; Vasile, A.; Blunt, M.J.; Niasar, V.; Marone, F.; Schmidt, T.J.; Büchi, F.N.; Eller, J. Operando Liquid Pressure Determination in Polymer Electrolyte Fuel Cells. *ACS Applied Materials & Interfaces* **2021**, *13*, 34003–34011.
49. Sepe, M.; Satjaritanun, P.; Hirano, S.; Zenyuk, I.V.; Tippayawong, N.; Shimpalee, S. Investigating Liquid Water Transport in Different Pore Structure of Gas Diffusion Layers for PEMFC Using Lattice Boltzmann Method. *Journal of The Electrochemical Society* **2020**, *167*, 104516.
50. Ye, Q.; Van Nguyen, T. Three-dimensional simulation of liquid water distribution in a PEMFC with experimentally measured capillary functions. *Journal of the Electrochemical Society* **2007**, *154*, B1242.
51. Khan, Z.A.; Salaberri, P.A.G.; Heenan, T.M.; Jarvis, R.; Shearing, P.R.; Brett, D.; Elkamel, A.; Gostick, J.T. Probing the structure-performance relationship of lithium-ion battery cathodes using pore-networks extracted from three-phase tomograms. *Journal of The Electrochemical Society* **2020**, *167*, 040528.
52. Goshtasbi, A.; García-Salaberri, P.; Chen, J.; Talukdar, K.; Sanchez, D.G.; Ersal, T. Through-the-membrane transient phenomena in PEM fuel cells: A modeling study. *Journal of The Electrochemical Society* **2019**, *166*, F3154.
53. Liu, C.P.; Saha, P.; Huang, Y.; Shimpalee, S.; Satjaritanun, P.; Zenyuk, I.V. Measurement of Contact Angles at Carbon Fiber–Water–Air Triple-Phase Boundaries Inside Gas Diffusion Layers Using X-ray Computed Tomography. *ACS Applied Materials & Interfaces* **2021**, *13*, 20002–20013.
54. Tranter, T.; Gostick, J.; Burns, A.; Gale, W. Capillary hysteresis in neutrally wettable fibrous media: a pore network study of a fuel cell electrode. *Transport in porous media* **2018**, *121*, 597–620.
55. Flückiger, R. Transport phenomena on the channel-rib scale of polymer electrolyte fuel cells. PhD thesis, ETH Zurich, 2009.
56. García-Salaberri, P.A.; Vera, M.; Zaera, R. Nonlinear orthotropic model of the inhomogeneous assembly compression of PEM fuel cell gas diffusion layers. *International Journal of Hydrogen Energy* **2011**, *36*, 11856–11870.
57. Hwang, G.; Weber, A. Effective-diffusivity measurement of partially-saturated fuel-cell gas-diffusion layers. *Journal of The Electrochemical Society* **2012**, *159*, F683.
58. Rosen, T.; Eller, J.; Kang, J.; Prasianakis, N.I.; Mantzaras, J.; Büchi, F.N. Saturation dependent effective transport properties of PEFC gas diffusion layers. *Journal of The Electrochemical Society* **2012**, *159*, F536.
59. Nam, J.H.; Kaviany, M. Effective diffusivity and water-saturation distribution in single-and two-layer PEMFC diffusion medium. *International Journal of Heat and Mass Transfer* **2003**, *46*, 4595–4611.
60. Flückiger, R.; Freunberger, S.A.; Kramer, D.; Wokaun, A.; Scherer, G.G.; Büchi, F.N. Anisotropic, effective diffusivity of porous gas diffusion layer materials for PEFC. *Electrochimica acta* **2008**, *54*, 551–559.
61. Hinebaugh, J.; Fishman, Z.; Bazylak, A. Unstructured pore network modeling with heterogeneous PEMFC GDL porosity distributions. *Journal of The Electrochemical Society* **2010**, *157*, B1651.
62. Lamibrac, A.; Roth, J.; Toulec, M.; Marone, F.; Stampanoni, M.; Büchi, F. Characterization of liquid water saturation in gas diffusion layers by X-ray tomographic microscopy. *Journal of The Electrochemical Society* **2015**, *163*, F202.
63. Kim, S.; Mench, M. Investigation of temperature-driven water transport in polymer electrolyte fuel cell: phase-change-induced flow. *Journal of The Electrochemical Society* **2009**, *156*, B353.

64. Belgacem, N.; Prat, M.; Pauchet, J. Coupled continuum and condensation–evaporation pore network model of the cathode in polymer-electrolyte fuel cell. *International Journal of Hydrogen Energy* **2017**, *42*, 8150–8165.
65. Aghighi, M.; Gostick, J. Pore network modeling of phase change in PEM fuel cell fibrous cathode. *Journal of Applied Electrochemistry* **2017**, *47*, 1323–1338.
66. Pasaogullari, U.; Wang, C.Y. Two-phase transport and the role of micro-porous layer in polymer electrolyte fuel cells. *Electrochimica Acta* **2004**, *49*, 4359–4369.
67. Prat, M.; Agaësse, T. Thin porous media. *Handbook of porous media* **2015**, pp. 89–112.
68. Zhou, J.; Putz, A.; Secanell, M. A mixed wettability pore size distribution based mathematical model for analyzing two-phase flow in porous electrodes. *Journal of The Electrochemical Society* **2017**, *164*, F530.
69. Sweijen, T.; Hassanizadeh, S.M.; Chareyre, B. Unsaturated flow in a packing of swelling particles; a grain-scale model. *Advances in Water Resources* **2020**, *142*, 103642.
70. Basu, S.; Wang, C.Y.; Chen, K.S. Phase change in a polymer electrolyte fuel cell. *Journal of The Electrochemical Society* **2009**, *156*, B748.
71. Satjaritanun, P.; Hirano, S.; Shum, A.D.; Zenyuk, I.V.; Weber, A.Z.; Weidner, J.W.; Shimpalee, S. Fundamental understanding of water movement in gas diffusion layer under different arrangements using combination of direct modeling and experimental visualization. *Journal of The Electrochemical Society* **2018**, *165*, F1115.
72. LaManna, J.M.; Chakraborty, S.; Gagliardo, J.J.; Mench, M.M. Isolation of transport mechanisms in PEFCs using high resolution neutron imaging. *International journal of hydrogen energy* **2014**, *39*, 3387–3396.
73. Wu, R.; Zhu, X.; Liao, Q.; Wang, H.; Ding, Y.d.; Li, J.; Ye, D.d. A pore network study on the role of micro-porous layer in control of liquid water distribution in gas diffusion layer. *international journal of hydrogen energy* **2010**, *35*, 7588–7593.
74. Koresawa, R.; Utaka, Y. Precise measurement of effective oxygen diffusivity for microporous media containing moisture by review of galvanic cell oxygen absorber configuration. *International Journal of Heat and Mass Transfer* **2014**, *76*, 549–558.
75. Kundu, S.; Fowler, M.; Simon, L.; Grot, S. Morphological features (defects) in fuel cell membrane electrode assemblies. *Journal of Power Sources* **2006**, *157*, 650–656.
76. Simon, C.; Hasché, F.; Gasteiger, H.A. Influence of the gas diffusion layer compression on the oxygen transport in PEM fuel cells at high water saturation levels. *Journal of The Electrochemical Society* **2017**, *164*, F591.
77. Qin, Y.; Ma, S.; Chang, Y.; Liu, Y.; Yin, Y.; Zhang, J.; Liu, Z.; Jiao, K.; Du, Q. Modeling the membrane/CL delamination with the existence of CL crack under RH cycling conditions of PEM fuel cell. *International Journal of Hydrogen Energy* **2021**, *46*, 8722–8735.
78. Baumgartner, W.R.; Parz, P.; Fraser, S.; Wallnöfer, E.; Hacker, V. Polarization study of a PEMFC with four reference electrodes at hydrogen starvation conditions. *Journal of Power Sources* **2008**, *182*, 413–421.
79. Takeuchi, N.; Fuller, T.F. Modeling and investigation of design factors and their impact on carbon corrosion of PEMFC electrodes. *Journal of The Electrochemical Society* **2008**, *155*, B770.
80. García-Salaberri, P.A.; Zenyuk, I.V.; Hwang, G.; Vera, M.; Weber, A.Z.; Gostick, J.T. Implications of inherent inhomogeneities in thin carbon fiber-based gas diffusion layers: A comparative modeling study. *Electrochimica Acta* **2019**, *295*, 861–874.
81. Hack, J.; García-Salaberri, P.A.; Kok, M.D.; Jarvis, R.; Shearing, P.R.; Brandon, N.; Brett, D.J. X-ray micro-computed tomography of polymer electrolyte fuel cells: What is the representative elementary area? *Journal of The Electrochemical Society* **2020**, *167*, 013545.
82. Zhan, Z.; Wang, C.; Fu, W.; Pan, M. Visualization of water transport in a transparent PEMFC. *International Journal of Hydrogen Energy* **2012**, *37*, 1094–1105.
83. Lu, Z.; Daino, M.M.; Rath, C.; Kandlikar, S.G. Water management studies in PEM fuel cells, part III: Dynamic breakthrough and intermittent drainage characteristics from GDLs with and without MPLs. *International Journal of Hydrogen Energy* **2010**, *35*, 4222–4233.
84. Quesnel, C.; Cao, R.; Lehr, J.; Kietzig, A.M.; Weber, A.Z.; Gostick, J.T. Dynamic percolation and droplet growth behavior in porous electrodes of polymer electrolyte fuel cells. *The Journal of Physical Chemistry C* **2015**, *119*, 22934–22944.

85. Ira, Y.; Bakhshan, Y.; Khorshidimalahmadi, J. Effect of wettability heterogeneity and compression on liquid water transport in gas diffusion layer coated with microporous layer of PEMFC. *International Journal of Hydrogen Energy* **2021**, *46*, 17397–17413.
86. Wong, A.K.C.; Banerjee, R.; Bazylak, A. Tuning MPL intrusion to increase oxygen transport in dry and partially saturated polymer electrolyte membrane fuel cell gas diffusion layers. *Journal of the Electrochemical Society* **2019**, *166*, F3009.
87. Forner-Cuenca, A.; Biesdorf, J.; Manzi-Orezzoli, V.; Gubler, L.; Schmidt, T.J.; Boillat, P. Advanced water management in PEFCs: diffusion layers with patterned wettability III. Operando characterization with neutron imaging. *Journal of The Electrochemical Society* **2016**, *163*, F1389.